ELSEVIER

Coordination Chemistry Reviews
144 (1995) 199–244

COORDINATION CHEMISTRY REVIEWS

Orbital interactions, electron delocalization and spin coupling in iron–sulfur clusters

L. Noodleman [a], C.Y. Peng [a], D.A. Case [a], J.-M. Mouesca [b]

[a] *Department of Molecular Biology, MB1, The Scripps Research Institute, La Jolla, CA 92037, USA*
[b] *Departement de Recherche Fondamentale sur la Matiere Condensée, Centre d'Etudes Nucléaires de Grenoble, CEA, 85 X 38041 Grenoble, France*

Received 9 September 1994; in revised form 16 December 1994

Contents

Abstract

The interconnections among orbital interactions, electron delocalization and spin coupling in iron–sulfur clusters are reviewed, with special attention to the complex nature of spin and

SSDI 0010-8545(95)07011-7

orbital states in 4Fe4S complexes. We summarize the uses of broken symmetry density functional calculations and spin projection methods for extracting Heisenberg spin coupling and electron delocalization parameters, as well as for understanding charge distributions and orbital aspects of electronic structure. The value of spin projection coefficients for sorting out spin coupling patterns in complex systems is also emphasized. Among the systems examined are oxidized, high-potential, iron–sulfur proteins, 4Fe ferredoxin proteins and related synthetic complexes. By analysis of experimental hyperfine parameters, a detailed model of spin coupling for the "double cubane" P cluster of nitrogenase has been proposed in recent work based on Mössbauer, electron paramagnetic resonance (EPR) and X-ray structural data; there is one pairwise valence delocalized and one trapped valence cubane in the P (oxidized) state. In the area of electron transfer energetics, we have found that Heisenberg spin coupling and electron delocalization both contribute substantially to the redox potentials of 4Fe4S complexes, and Heisenberg coupling contributes to the difference in redox potential between 1Fe and 2Fe2S complexes, based on recent density functional calculations for model systems in solvents.

Keywords: Iron-sulfur clusters; Orbital interactions; Electron delocalization; Spin coupling.

---

1. Introduction

Iron–sulfur proteins, which were clearly recognized by biochemists only about 30 years ago, have been an important part of living creatures for a large fraction of the Earth's history [1]. These metalloproteins play a significant role in electron transfer and also in catalysis over the full range of living organisms, encompassing bacteria, plants and higher animals. They can have a variety of functions: (1) as single electron transfer agents in the mitochondrial electron transport chain in eukaryotic cells with coupling to energy transducing processes (proton pumping) across the mitochondrial inner membrane [2,3]; (2) in photosynthetic electron transport in plants and algae [4]; (3) as catalytic agents in (de)hydratases (where there is no net electron transfer from enzyme to substrate), of which aconitase (a mitochondrial enzyme of the Krebs cycle) is the best known example [5,6]; (4) as part of complex multielectron oxido-reductases where substrate binding and catalytic transformations are combined with multielectron transfers [7–10].

The state of the field has been periodically reviewed in the so-called "iron–sulfur books" [1–13], which also include information about synthetic model compounds that use organic thiolates in place of cysteine ligands from the protein [14]. Compared with the native FeS clusters in proteins, the synthetic structures can be accurately determined by X-ray diffraction, magnetic measurements can be more precise [15] and, in some cases, the orientation of the g tensor and the Fe hyperfine tensors determined by electron paramagnetic resonance (EPR) and electron-nuclear double resonance spectroscopy (ENDOR) can be related to the geometric orientation of the cluster [16,17]. The properties of the synthetic clusters can be usefully compared with those of FeS proteins, and considerable insight is then gained into which properties are intrinsic to the FeS clusters themselves, and which depend on the protein polypeptide environment.

A common motif of metalloprotein active sites is the presence of ligand-bridged transition metal centers which act as electron transfer or catalytic agents. In addition to the iron–sulfur proteins, these include cytochrome oxidase [8], the oxygen evolving complex (OEC) of photosystem II [10,18], manganese catalase [19] and hemerythrin-like two-iron centers, including the enzymes methane monoxygenase and ribonucleotide reductase [20,21]. Functionally, these play a vital role in coupling electron transfer to energy conserving processes in cells, and in performing various biosynthetic tasks. From the viewpoint of electronic structure, these systems, like iron–sulfur proteins, possess active sites where high-spin transition metal atoms are spin coupled via bridging and terminal ligands [14]. The catalytic and electron transfer events that occur when the protein interacts with its reaction partner are usually quite different from the more familiar processes of Lewis acid–base chemistry, and the catalytic cluster can act like a stable radical (or a diradical or polyradical) center. There is a large literature on the application of spin hamiltonian models to polynuclear transition metal clusters, including a number of excellent reviews [22–25]. A number of groups have also been active in applying quantum chemistry calculations, particularly to dinuclear transition metal complexes [26–34].

In this review, we describe the recent progress towards the development of unifying concepts that can aid in the interpretation of a variety of physical and spectroscopic results in iron–sulfur clusters. Section 2 discusses quantum chemistry calculations (using the broken symmetry molecular orbital model) which provide fundamental information about energy level schemes and the nature of the charge and spin distributions of various states. In Section 3, we outline the connections between the molecular orbital description and spin hamiltonian models which provide a compact description of the large number of low-lying excited states that can arise as a result of antiferromagnetic coupling between metal sites. This section also describes a spin projection "algebra" that relates observable parameters, such as hyperfine couplings and *g* tensors, to quantities that characterize the intrinsic properties of each metal site. Section 4 then applies these ideas to the four-iron cubane systems found in ferredoxins, aconitase and high-potential iron proteins, and to the 'double cubane" P cluster of nitrogenase.

2. Quantum chemistry calculations on iron–sulfur clusters

Applications of quantum chemistry to polynuclear iron–sulfur clusters have a long history, beginning with qualitative symmetry arguments [35,36], and including early molecular orbital calculations at the Hartree–Fock or Xα level [37–39]. The early spin polarized 1Fe models showed the importance of high-spin Fe for the electronic structure of $Fe(SR)_4$ systems [37,38]. By contrast, the early dinuclear and polynuclear models employed a spin restricted molecular orbital framework [35,36,39]. Although such models can be useful for obtaining a qualitative understanding of some aspects of optical spectra (but failing in other aspects), they have serious deficiencies in describing ground and low-lying excited states. (For example, the individual metal sites are low spin rather than high spin within a spin restricted framework.) The problems arise for much the same reason that molecular orbital theory fails for H_2 at large internuclear distances: when the overlap of atomic orbitals on two or more centers becomes very small, a molecular orbital description assigning electrons of both spins to each center is inappropriate. For iron–sulfur clusters, the iron d–d interactions are quite weak, and the closed-shell solution is unstable to perturbations that allow electron spins to localize at the iron centers. This lack of correlation between electrons of opposite spin leads to important effects, most notably a failure to predict the existence of low-lying paramagnetic excited states in the $[Fe_4S_4]^{3+}$ state or to rationalize the patterns of hyperfine interactions in odd-electron systems.

A practical method that can circumvent these problems and can interpolate between molecular orbital and valence bond limits uses the idea of spin and space unrestricted wavefunctions to provide an improved description of exchange correlation effects. These ideas were first applied to iron–sulfur clusters about 15 years ago, using the Xα-scattered wave approximation [40,41]. This level of computation has since been supplanted by more accurate (and expensive) methods, but the scattered wave model is actually quite reasonable for compact systems such as iron–sulfur clusters, and many of the early conclusions have been borne out by more recent calculations [42]. In this section, we give an overview of the applications of the broken symmetry model to iron–sulfur dimers and cubane-like systems, concentrating on relatively recent calculations that use modern density functional techniques.

2.1. Density functional calculations

Density functional theory is now becoming widely recognized as a high-level method for carrying out quantum chemistry calculations, particularly for transition metal clusters, which are difficult to handle by more conventional ab initio techniques [43,44]. Compared with ab initio methods, the distinctive feature of density functional theory is that both the exchange and correlation parts of the electronic energy are approximated by terms that depend only on functionals of the electron density. As with any quantum chemistry method, however, the results depend in an important fashion on the quality and flexibility of the basis set used. Because density functional methods scale as a lower power of basis set size than Hartree–Fock or more complex ab initio methods, large basis sets are often feasible with a density functional approach.

Recent improvements in density functional theory involve the introduction of non-local correction terms, which allow an improved description of molecular geometries, bond energies and vibrational frequencies. These non-local terms depend both upon α and β densities and their gradients. For small molecules, density functional methods usually give bond energies accurate to 3–5 kcal mol^{-1}, bond lengths accurate to 0.02 Å and bond angles accurate to a few degrees. In addition, accurate energies have been obtained for a variety of chemical reactions, excitation energies, electron affinities, proton affinities and ionization potentials [43].

Transition metal complexes provide greater challenges for all quantum chemical methods. Geometries and vibrational frequencies have been calculated with good accuracy in recent work (average bond length error, 0.03 Å) [45]. We have calculated bond energies for a variety of small, spin polarized, transition metal complexes ($MnCl_2$, $FeCl_2$, $FeCl_3$, ScO, TiO, VO, CuO), which gave bond energies with errors in the range 1%–17% (0.8–11 kcal mol^{-1}), in agreement with the findings of other groups (for example, on simple metal hydrides) [46]. This range of accuracy is also typical for ionization energies and excitation energies of transition metal atoms [47]. When we compare these results with those achieved with ab initio methods, we find that they are considerably better than Hartree–Fock, and as good as second-order Moller–Plesset (MP2) results, while the computational efficiency is much greater. Because of this, much larger systems are feasible with density functional methods, and we can also use very high quality basis sets (typically of triple ζ quality on the transition metals and double or triple ζ on the ligand atoms).

The best currently available non-local (i.e. gradient based) exchange correlation potentials are associated with the names of Becke (B) for exchange and Perdew (P), Stoll (S) or Lee, Yang and Parr (LYP) for correlation [43,48]. These are added to the local potential due to Vosko, Wilk and Nusair (V). Most of our recent calculations are either of Vosko–Becke–Perdew (VBP) or Vosko–Stoll–Becke (VSB) type. There are continuing efforts in testing and improving new density functionals [48]. The calculations reviewed here have mostly used the Amsterdam density functional (ADF) codes developed in the laboratory of E.J. Baerends [49]. The ADF codes expand orbitals in a basis of Slater-type orbitals (STOs), which generally allows a more rapid convergence than gaussian basis expansions, at the expense of some computation time. Other large transition metal clusters have been investigated with this program set, including iron and cobalt porphyrins [50], metal phthalocyanines [51] and polynuclear manganese-oxo-carboxylate complexes [52].

2.2. *Application to iron–sulfur complexes*

Fig. 1 shows a schematic diagram of the structures of rubredoxin (1Fe) and ferredoxin (2Fe,4Fe) active sites $Fe(SR)_4$, $Fe_2S_2(SR)_4$ and $Fe_4S_4(SR)_4$. In proteins, R ≡ cysteine as depicted, and the cysteine residues are connected to the polypeptide chains of the protein. In synthetic systems, R is an organic ligand which may be covalently bonded to a particular terminal sulfur, bonded to two sulfurs, as in S_2–*o*-xylyl [53], or to three sulfurs, as in recently synthesized trithiol (LS_3) ligands, useful in making site differentiated clusters [54].

Some special techniques are required to apply density functional calculations to spin coupled systems where there are (formally) a large number of unpaired electrons. Most of these systems are antiferromagnetically coupled, but the total spin of the ground state (or low-lying excited states) is not obvious, nor is the composition of the total spin in terms of subunits evident in polynuclear systems. Furthermore, there is a close connection between electron delocalization and spin coupling. We have constructed a novel broken symmetry method which is well adapted for treating high-spin transition metal sites that are spin coupled via bridging ligands, and where metal–ligand covalency must be realistically represented [55]. These may also be

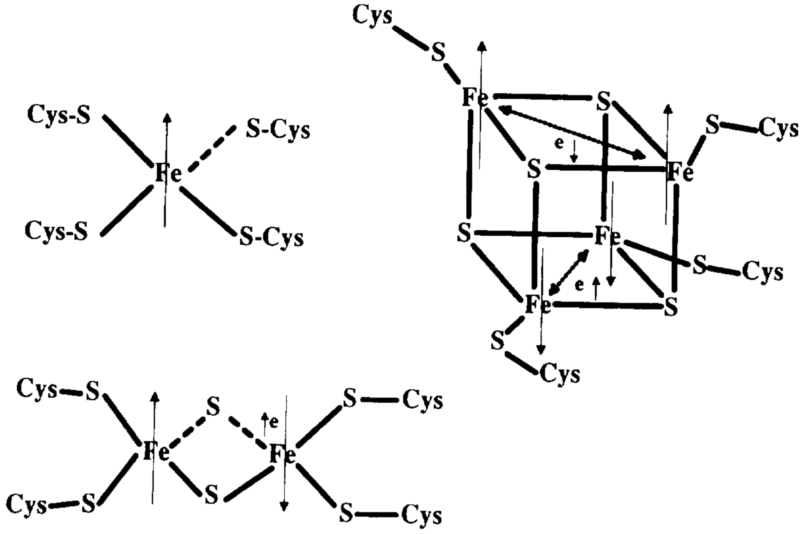

Fig. 1. Schematic diagram of the structures and spin alignments for $[Fe(SR)_4]^{1-}$ (oxidized form), $[Fe_2S_2(SR)_4]^{3-}$ (reduced form) and $[Fe_4S_4(SR)_4]^{2-}$ with R ≡ S-cysteine (oxidized ferrodoxin). The large spin vectors represent high-spin $S_i = 5/2$ spin vectors on the Fe_i sites. The smaller spins represent additional electrons of opposite spin $s_i = 1/2$ which can combine with the larger spins to give high-spin ferrous $S_i = 2$ on some sites, leaving the remaining sites as $S_i = 5/2$ (high-spin ferric). In the 4Fe4S systems, there are two delocalized mixed valence pairs, each with aligned site spin vectors.

referred to as density functional valence bond calculations since the energies and properties of pure spin states can be extracted from the theory by the use of spin coupling algebra.

In the spin polarized version of density functional theory, the spin-up (α) and spin-down (β) electrons are treated separately, and this is critical for high-spin transition metal sites, indeed for any system with significant spin density (defined as the local difference $\rho_\alpha - \rho_\beta$ of the α and β electron densities). The electrons move in a self-consistent field (SCF) potential due to all the electrons and nuclei, but one that is, in general, locally different for the spin α and spin β electrons. This is because electrons of the same spin will avoid each other "automatically" by virtue of the antisymmetry of the many-electron wavefunction (the Pauli principle), whereas electrons of opposite spin are not as effective in avoiding electron–electron repulsion. Where possible, then, opposite spin electrons can optimize their interactions by occupying different spatial orbitals. These spin-dependent spatial preferences appear as SCF potentials that have different shapes for α and β electrons. In general, the SCF potential stabilizes α electrons (relative to β) in regions of excess α spin density [55].

In the presence of weak field ligands, such as thiolates, this means that the iron majority spin electrons (those having a spin index, either α or β, which has the larger local density at that atom) are stabilized in energy, while the corresponding minority spin electrons are destabilized on the same center. (This destabilization holds true for the minority spin orbitals, whether or not these are occupied levels.) The Fe(3d) shell is quite compact, and the energy splitting between majority spin and minority spin electrons is very large (of the order of 4–5 eV for Fe^{3+}) [55,56]. The spin polarization energy of high-spin iron substantially exceeds the ligand field stabilization energy that would be available to low-spin iron sites, so that this competition strongly favors high-spin metal sites. This large energy splitting between majority and minority spin 3d energy levels also means that simple molecular orbital pictures that ignore spin polarization effects (such as in extended Hückel theory) can lead to misleading descriptions of the balance of forces in high-spin transition metal complexes.

The large vectors shown in Fig. 1 denote majority spin vectors, representing the majority spin electrons. Each large spin vector shows an iron site spin of magnitude $S_i = 5/2$ (total spin quantum number on the Fe site i, which may include some delocalized spin density on the nearby ligands), and this corresponds to a high-spin ferric site. The smaller vectors denote individual minority spin electrons which may be present, since these complexes may have some combination of high-spin ferric (Fe^{3+}, five valence electrons) and ferrous (Fe^{2+}, six valence electrons) sites. In addition, truly intermediate, delocalized, mixed valence ($Fe^{2.5+}$) sites may be present, as found in 4Fe systems. Each smaller spin vector is always of opposite sign to the large spin vector on the same iron site (or on pairs of parallel spin sites), since the Fe(3d) shell is always at least half full. Some of the large spin vectors are parallel aligned, and others are antiparallel aligned. Later, we will present an analysis of the energy terms contributing to parallel or antiparallel alignment of site spin vectors.

2.3. Ligand field states in spin polarized systems

The principal ligand field states of high-spin ferrous sites are derived from minority spin orbitals, which reside mainly on the metal sites, but have significant metal–ligand covalency involving both bridging and terminal ligands. In a roughly tetrahedral ligand field, the ligand field orbitals are e and t_2 (in point group T_d) for the weakly antibonding (M—L π^*) and strongly antibonding (M—L σ^*) metal–ligand orbitals respectively; in lower site symmetry (C_{2v}), these transform as $e \rightarrow a_1, a_2$ and $t_2 \rightarrow b_2, a_1, b_1$. The lowest lying of these a_1 orbitals is σ to the Fe–Fe axis in both 2Fe and 4Fe systems. It is important to realize that ligand field orbitals can be either metal–metal bonding (lower energy) or metal–metal antibonding (higher energy), while being simultaneously metal–ligand antibonding. The metal–metal interactions become particularly significant for those pairs whose spin vectors are parallel aligned. Furthermore, the ligand field orbitals derived from the weakly antibonding $e \rightarrow a_1, a_2$ are the most important for the energetics of the ground and low-lying excited electronic (and spin) states. This is because the orbitals derived from e are of the correct energy to be the highest occupied or lowest unoccupied in both mononuclear and polynuclear complexes; the t_2 derived levels are too high in energy to be part of the occupied (or lowest unoccupied) level set, and this is not changed by metal–metal interactions. These conclusions have been obtained from our quantitative density functional calculations on iron–sulfur complexes with one to four irons, but the results are clearly quite consistent with the general ideas of ligand field theory [57,58] and the theory of metal–metal bonding interactions [59]. There are, however, a number of subtle issues involved in the analysis of metal–ligand and metal–metal bonding interactions in the presence of high-spin metal sites and spin coupling interactions.

2.4. *Energy level structure and the inverted level scheme*

One important question is where do the S(3p) energy levels lie relative to the Fe(3d) levels? Fig. 2 gives the energy level structure for the antiferromagnetically aligned, broken symmetry state of an oxidized 2Fe2S cluster $Fe_2S_2(SR)_4{}^{2-}$ ($R \equiv CH_3$), calculated with a VBP exchange correlation potential. The vertical axis gives the orbital energies and the horizontal axis separates levels according to their spin index (α or β) as well as their principal spatial location (on the left, middle or right of the molecule, as shown in Fig. 1). While the geometric symmetry of the model system is D_{2d}, in the broken symmetry state, the antiferromagnetic alignment

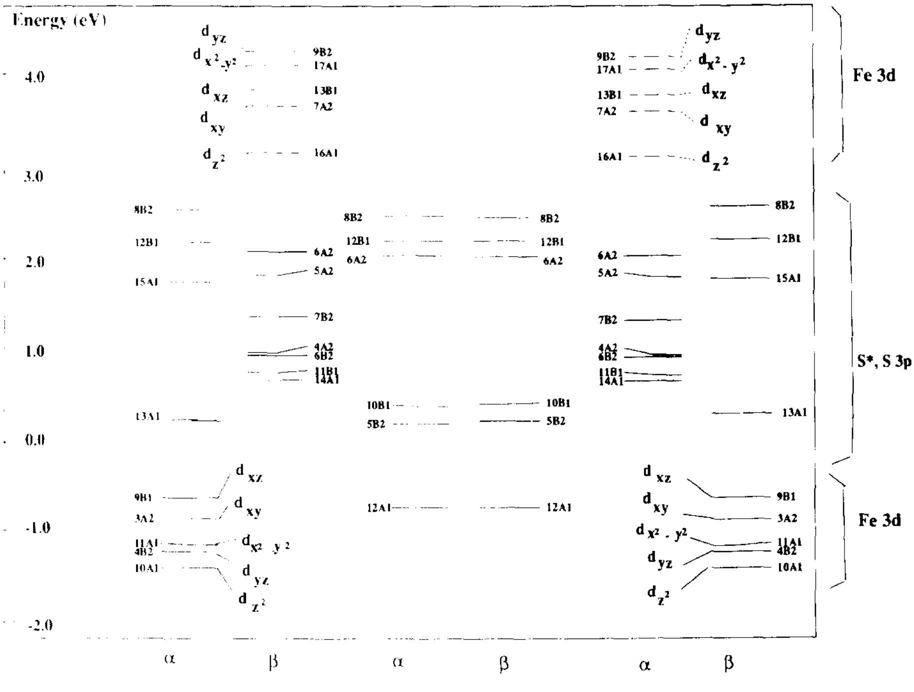

Fig. 2. Energy level diagram for the broken symmetry (BS) state of $[Fe_2S_2(SCH_3)_4]^{2-}$ as calculated with a density functional Vosko–Becke–Perdew (VBP) potential. Spin-up (α) and spin-down (β) levels are indicated by the column label (see bottom panel). Filled levels are given by the full lines, with empty (ligand field) levels given by the broken lines. The orbitals are also grouped horizontally by their spatial location on the left, center or right ($(RS)_2Fe–S_2{}^*–Fe(SR)_2$) of the molecule (see also the structural diagram, Fig. 1). The filled majority spin Fe(3d) levels along with S,S*(3p) are shown. The minority spin Fe(3d) levels (empty) lie higher, and the character of each Fe orbital is shown. The Fe–Fe axis is z, the $Fe_2S_2{}^*$ bridge plane is yz and the $Fe(SR)_2$ terminal plane is xz.

of the spins leads to the lower electronic symmetry of C_{2v}, so that the left and right sides of the molecule become inequivalent. As in Fig. 1, the majority spin Fe levels are spin-up (α) on the left and spin-down (β) on the right, and these levels are stabilized by exchange interaction and have low energies. The filled terminal and bridging sulfur (S,S*)(3p) derived levels lie between the occupied majority spin Fe(3d) levels and the unoccupied (or partially occupied) minority spin Fe(3d) levels (above the broken line).

The minority spin Fe(3d) orbitals display the energy splitting pattern expected for M—L antibonding ligand field orbitals described above. (By contrast, the majority spin Fe(3d) levels show a different splitting pattern and are M—L bonding.) Like the majority spin levels, the minority spin orbitals are largely localized to the left or right depending on the spin index α or β. The iron–sulfur complexes display significant metal–ligand covalency, so that mainly Fe energy levels can have 20%–40% ligand (mainly S,S*) character, and conversely for mainly S,S* levels.

A similar level pattern, with Fe(3d) majority spin orbitals lying below S,S*(3p) levels, which in turn lie below Fe(3d) minority spin levels, applies to all the $Fe(SR)_4{}^{1-,2-}$, $Fe_2S_2(SR)_4{}^{2-,3-}$ and $Fe_4S_4(SR)_4{}^{1-,2-,3-}$ complexes. This pattern of energy levels is called the "inverted level scheme" to distinguish it from the "normal level scheme". In the "normal level scheme", appropriate to some low-spin transition metal complexes [60,61], all occupied metal levels lie above all occupied ligand levels, and the lowest unoccupied levels are also metal in character. In dinuclear transition metal complexes with low-spin metal sites (organometallic systems), the "normal level scheme" is followed in some systems (such as $Fe_2(CO)_9$, $Fe_2(CO)_6(PPh_2)_2{}^{0,2-}$ and $Co_2(CO)_6C_2H_2$) and not in others (e.g. $Fe_2(CO)_6S_2{}^{0,2-}$), even where these are related in structure and other electronic features [61]. If the highest occupied levels and/or the lowest unoccupied levels are highly covalent (i.e. there is thorough mixing of metal–ligand character in these molecular orbitals, or metal and ligand levels are closely spaced in this energy region), we can call this the "mixed level scheme" (e.g. $Fe_2(CO)_6S_2{}^{0,2-}$) [61]. Another example of a system obeying the "mixed level scheme" for a spin polarized and spin coupled cluster is the tetranuclear manganese cubane complex treated in Ref. [52].

In iron–sulfur complexes, the strong spin polarization of high-spin Fe sites combines with the energies of the S(3p) band of the bridging sulfur and terminal thiolates (which are destabilized by their anionic character) to produce this inverted pattern. Experimental confirmation of the inverted level scheme in $FeSR_4{}^{1-}$ and $FeCl_4{}^{1-}$ has been obtained by Solomon's group using a combination of photoelectron, polarized absorption and magnetic circular dichroism spectroscopies [62–65]. For example, there is strong charge transfer character in the lowest lying spin forbidden transition of the ferric thiolate complex, which formally would be spin forbidden Fe d → d from a simple ligand field perspective. There are also low-lying S,S* → Fe spin allowed (and dipole allowed) charge transfer transitions, consistent with the inverted level scheme.

2.5. Electron relaxation on oxidation or reduction

The phenomenon of electron relaxation is an important aspect of metal–ligand covalency. It is often underappreciated because it exemplifies, along with spin polarization, the limitations of the frontier orbital picture of electronic structure. Frontier molecular orbital theory focuses on the energies and character of the highest occupied (HOMO) and lowest unoccupied (LUMO) molecular orbitals as the controlling features of reactivity. Spin polarization shows that low-lying orbitals can have an important net influence both on the system spin and on the character and delocalization of the higher lying minority spin orbitals. Electron relaxation shows that orbitals other than the "active" ones (HOMO and LUMO) can have substantial cumulative effects. Both covalency and relaxation are well established in transition metal complexes [37,38,40,56,66], and they are inherent in the self-consistent field framework. Metal–ligand covalency can be manifest through direct mixing of metal and ligand atomic orbitals in the molecular orbitals, or through electron relaxation effects. During an oxidation or reduction process, the electron and spin density may change both by altering the occupation of the single "active" orbital (which accepts or gives up an electron) and also by changes in the remaining "passive" orbitals (electron relaxation). Our calculations show that electron relaxation effects are quite large in FeS systems. In most redox events, an electron is added (or subtracted) from a mainly metal orbital. Although there are significant changes in the electron density distribution at the corresponding Fe sites, as shown by Mössbauer spectroscopy (consistent with predictions from density functional calculations) [67], most of the change in net charge is found to be spread over the bridging and terminal sulfurs [55,56,67]. This is shown in electron density difference maps for 2Fe2S complexes [56].

In Fig. 3, we show an electron density difference map for the reduced minus oxidized model 2Fe2S cluster calculated from the broken symmetry states with a VBP potential. The reduced half of the complex is the lower part of the plot. The asymmetric change in the charge distribution at Fe is clear, showing an increased density in $\mathrm{Fe(3d)}_{z^2})_{\mathrm{red}}$ (full contours), along with an increased density on reduction at all terminal sulfurs (and methyl groups). The largest density increase shown is on the $\mathrm{S}_{\mathrm{red}}$ atoms and on $(\mathrm{CH}_3)_{\mathrm{red}}$ (see also Table 1). (The bridging S* atoms also show a population increase on reduction.)

For 4Fe4S complexes, we have obtained color, three-dimensional (3-D), electron density difference maps of the charge flow on oxidation or reduction of $4\mathrm{Fe}4\mathrm{S}^{3+,2+}$ and $4\mathrm{Fe}4\mathrm{S}^{2+,1+}$ clusters with the model thiolate as $\mathrm{SR} \equiv \mathrm{SCH}_3$ [55]. This corresponds well with the pattern of increased N—H- - -S hydrogen bonding found on reduction of 4Fe4S clusters in proteins. In a more extreme example, protonation of a bridging μ_2-S is observed on $3\mathrm{Fe}4\mathrm{S}^{1+,0}$ reduction at low pH in a protein, consistent with very substantial changes in electron density at S* [68].

A numerical measure of the extent of these relaxation changes can be obtained by defining effective atomic populations in various oxidation states. Although there is no rigorous way to divide charge among atoms, it is often useful to consider so-called "electrostatic potential" (ESP) charges [69–73]. These are obtained by a least-squares fitting procedure, so that the potential arising from the effective partial charge distribution matches as well as possible the potential arising from the full wavefunction. The comparisons are made at points outside the van der Waals' envelope of the molecule or cluster, because the most common application of these

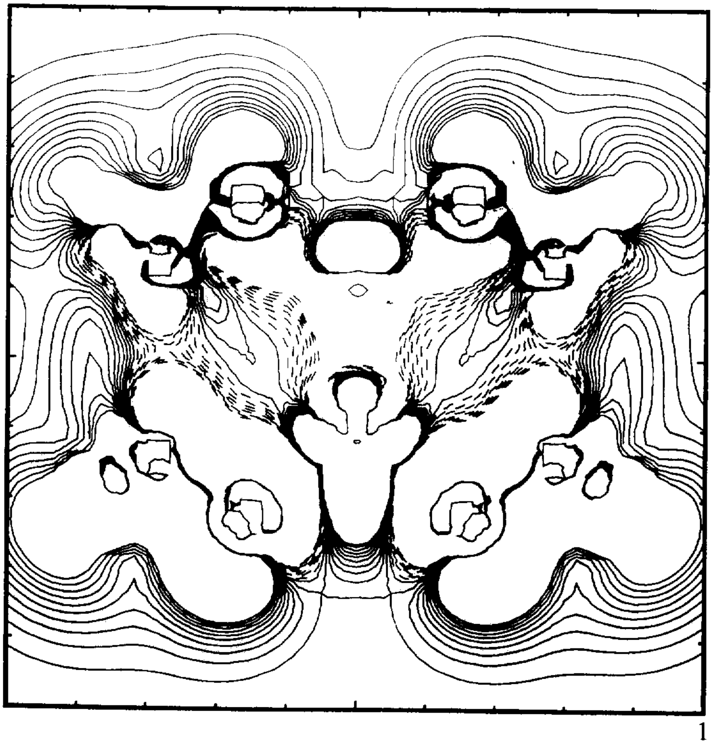

Fig. 3. An electron density difference map for the reduced minus oxidized model 2Fe2S cluster calculated from the broken symmetry states with a VBP potential. The plot is made in the $(SR)_2Fe_2(SR)_2$ plane (xz). The Fe–Fe (z) axis is vertical through the center of the plot. The reduced half of the complex is the lower part of the plot. The asymmetric change in the change distribution at Fe is clear, along with the increased density on reduction at all terminal sulfurs (and methyl groups), given by the full contour lines. The largest density increase is on the S_{red} atoms and on $(CH_3)_{red}$ (see also Table 1).

Table 1
Charges and spin populations for 1Fe and 2Fe systems

$[Fe(SCH_3)_4]^{2-/1-}$					$[Fe_2S_2^*(SCH_3)_4]^{3-/2-}$				
Atom	ESP charges		Spin populations		Atom	ESP charges		Spin populations	
	2−	1−	2−	1−		3−	2−	3−	2−
Fe	+0.900	+0.813	+3.338	+3.577	Fe_{ox}	+0.907	+0.761	+3.256	+3.119
S	−0.708	−0.507	+0.159	+0.326	Fe_{red}	+0.818	+0.761	−2.847	−3.119
CH_3	−0.017	+0.054	+0.006	+0.032	S*	−0.780	−0.614	+0.174	0.000
					S_{ox}	−0.731	−0.590	+0.187	+0.235
					S_{red}	−0.804	−0.590	−0.100	−0.235
					CH_{3ox}	−0.013	+0.015	+0.028	+0.026
					CH_{3red}	−0.034	+0.015	+0.007	−0.026

effective charge distributions is to estimate the electrostatic interactions between the cluster and other nearby charges, such as those in the surrounding protein.

We have determined ESP charge models for a variety of iron–sulfur clusters in various oxidation states, and the results are given in Tables 1 and 2. (These calculations were performed with a Vosko–Stoll potential plus Becke energy correction term, and are referred to as VS + B [70].) These should be useful for molecular mechanics or dynamics simulations of iron–sulfur proteins, and also provide one picture of the way in which electron relaxation occurs. For example, the charge on each sulfur increases (becomes more negative) by about $-0.2e^-$ on one electron reduction of the $Fe(SR)_4{}^{1-}$ system. Comparable changes of $-0.15e^-$ to $-0.2e^-$ per sulfur atom are observed for reduction of $Fe_2S_2(SR)_4{}^{2-}$, and charge differences of about $-0.15e^-$ for each S or S* are seen for each one electron reduction event in the $Fe_4S_4(SR)_4{}^{1-}$ (or 2−) system. This leaves very little in the way of additional electronic charge for the iron sites on reduction. Most of the $1e^-$ added has gone to the sulfurs, and is fairly uniformly divided over these, consistent with increased N—H— —S hydrogen bonding in Fe—S proteins on reduction. (There is still a small left–right charge asymmetry in the 2Fe systems on reduction, and a small top–bottom charge asymmetry for the odd-electron 4Fe systems.) Surprisingly, the positive charge on Fe typically increases slightly on reduction, even where this is the Fe site formally reduced. In fact, the main changes in the electronic distribution at Fe, based on our calculations, are in the shape and anisotropy of the electron density, particularly the Fe(3d) density, not in the net charge [55,56]. There is a small increase in Fe(3d) net population on reduction (by Mulliken or charge partitioning analysis) [56,67], consistent with increases in Mössbauer isomer shifts for reduced Fe sites, but the changes in Fe(3d) anisotropy (as monitored by Mössbauer quadrupole splittings) are much larger [74,75]. The ESP charges in Tables 1 and 2 also show substantial Fe—S and Fe—S* bond polarity, with the Fe sites positive and S,S* negative, but with much smaller charges than indicated by the formal Fe^{2+}, Fe^{3+} and S^{2-} charges. In this respect, the ESP charges are also more polar than the Mulliken charges, but the charge differences on reduction are very comparable with the two methods.

3. Broken symmetry method for spin coupled systems

Although the density functional methods outlined above provide a powerful way to obtain fundamental information about the energetics and electron distributions in iron–sulfur clusters, there are distinct problems in describing the ground and excited states of most spin coupled systems. This is because the ground state wavefunctions of these systems are not close to a single determinant of molecular orbitals, and can only be represented by a multiconfiguration wavefunction (and corresponding electron density). In fact, the spin-up, spin-down "arrow" representation in Fig. 1 looks more like a valence bond description than a molecular orbital description. Because of the large amount of metal–ligand covalency, a simple VB picture also fails to capture the primary aspects of the electron distribution.

Table 2
Charges and spin populations for $[Fe_4S_4^*(SCH_3)_4]^{3-,2-,1-}$

A: ESP charges

Atom	3−		2−	1−		
	OC1	OC2	REF	OS1	OS2	OS3
Fe_{ox}	+0.518	+0.484	+0.409	+0.304	+0.286	+0.343
Fe_{red}	+0.460	+0.481	+0.409	+0.321	+0.340	+0.326
S_{ox}^*	−0.576	−0.542	−0.393	−0.233	−0.323	−0.249
S_{red}^*	−0.513	−0.523	−0.393	−0.238	−0.267	−0.260
S_{ox}	−0.716	−0.710	−0.567	−0.398	−0.383	−0.416
S_{red}	−0.707	−0.724	−0.567	−0.429	−0.416	−0.419
CH_{3ox}	+0.028	+0.020	+0.050	+0.084	+0.089	+0.086
CH_{3red}	+0.007	+0.014	+0.050	+0.089	+0.085	+0.090

B: Mulliken charges

Atom	3−		2−	1−		
	OC1	OC2	REF	OS1	OS2	OS3
Fe_{ox}	+0.087	+0.089	+0.021	−0.044	−0.034	+0.009
Fe_{red}	+0.071	+0.070	+0.021	−0.016	−0.011	−0.011
S_{ox}^*	−0.354	−0.346	−0.206	−0.080	−0.093	−0.119
S_{red}^*	−0.323	−0.322	−0.206	−0.081	−0.100	−0.097
S_{ox}	−0.329	−0.331	−0.211	−0.082	−0.071	−0.093
S_{red}	−0.325	−0.338	−0.211	−0.100	−0.103	−0.096
CH_{3ox}	−0.157	−0.158	−0.105	−0.047	−0.043	−0.044
CH_{3red}	−0.169	−0.163	−0.105	−0.050	−0.046	−0.049

C: Spin populations

Atom	3−		2−	1−		
	OC1	OC2	REF	OS1	OS2	OS3
Fe_{ox}	+2.886	+2.835	+2.668	+2.086	+2.130	+2.858
Fe_{red}	−2.550	−2.472	−2.668	−2.502	−2.513	−2.541
S_{ox}^*	+0.186	+0.120	−0.001	−0.090	−0.066	+0.077
S_{red}^*	−0.049	−0.026	+0.001	−0.006	+0.055	+0.049
S_{ox}	+0.140	+0.137	+0.185	+0.209	+0.130	+0.285
S_{red}	−0.125	−0.092	−0.185	−0.200	−0.226	−0.232
CH_{3ox}	+0.010	+0.010	+0.014	+0.019	+0.014	+0.022
CH_{3red}	+0.001	−0.013	−0.014	−0.015	−0.021	−0.019

The broken symmetry approach for spin polarized and spin coupled systems, in combination with spin projection methods, provides an intuitive picture of the energetic interactions which contains most of the physics involved. The basic idea is to construct "broken symmetry" single determinant wavefunctions, which are not pure spin states, and therefore are not expected to represent the true wavefunctions of the system. Rather, spin projection techniques are used to estimate the energies and properties of the "correct" pure spin states. This represents a synthesis of density functional ideas with the ideas of broken space and spin symmetry perhaps best exemplified by Lowdin's "symmetry dilemma" from the 1950–1960s and his different orbitals for different spin (DODS) methods [76,77a]. Earlier important work includes that of Coulson and Fischer [77b] on the dissociation of H_2, while contemporaneous and later work includes that of Nesbet [78,79], Anderson [80,81] and Hay [82]. Fukatome [83] has summarized and carefully developed the unrestricted approach for H_2 dissociation. In the 1970–1980s, similar ideas were shown to be relevant for single and multiple metal–metal bonds, where the weaker δ and δ^* components can break space and spin symmetry to form an overlapping valence bond pair [82,84,85].

We represent an antiferromagnetic spin coupled state (broken symmetry state) within density functional theory as analogous to a spin unrestricted determinant in which spin-up electrons are predominantly located on some metal sites and spin-down electrons on others [55,86]. It is called a broken symmetry state because the electronic symmetry is often lower than that of the nuclear geometry. The broken symmetry method has been applied to a number of other transition metal complexes, in most cases within the density functional framework [32–34,87]; however, there are some recent examples in which the application of the broken symmetry method within an ab initio unrestricted Hartree–Fock (UHF) (with an open-shell restricted Hartree–Fock (ROHF) representation of the high-spin state) has been demonstrated in various transition metal complexes [88–90]. Prominent among the density functional applications of the spin polarized broken symmetry method has been work on dicopper peroxide model complexes related to the active sites of oxy-hemocyanin and tyrosinase [34], and on model complexes for the diferric active site related to hemerythrin [87]. In addition, there are applications to copper dimer (d^9–d^9) and copper–vanadium dimer complexes in both the strong metal–metal bonding and weak bonding limits [32,33]. Here we show how these ideas can be applied to iron–sulfur clusters.

3.1. Examination of broken symmetry in spin coupled dimers

The concept of broken symmetry has both conceptual and computational advantages. From a conceptual viewpoint, it is helpful to separate orbital aspects of electronic structure from the specification of detailed pure spin states. However, there is always a link between spin and orbital degrees of freedom in such systems, and the goal is to describe the phenomenon in the most compact way. The broken symmetry (BS) state represents an "averaged" antiferromagnetic (AF) alignment of spins, while the high-spin state gives a ferromagnetic (F) alignment. From a computational viewpoint, it is very difficult to represent pure spin states in a spin coupled system within density functional theory, but the representation of broken symmetry states is straightforward.

A density functional high-spin (HS) state is analogous to a (UHF) high-spin state. The α orbitals are different from those of β spin, but both sets obey the overall molecular symmetry; Fig. 4 gives the energy levels for the D_{2h} model of the oxidized 2Fe2S cluster, again with a VBP exchange correlation potential. The minority spin Fe(3d) orbitals are entirely delocalized over both Fe centers, forming bonding or antibonding combinations of Fe(3d) orbitals, and including some ligand interaction as well. The relevant delocalized orbitals are shown in Fig. 5. This is in strong contrast with the localized character of Fe minority spin orbitals in the BS state; the latter is a direct consequence of the antiparallel alignment of Fe site spin vectors, while parallel alignment in HS allows full Fe–Fe delocalization.

For the ground state of a 2Fe2S dimer, the spin-up electrons reside mainly on one half of the molecule and spin-down electrons on the other half (antiparallel alignment of spins). A "high-spin" state can also be constructed where the spins of the cluster are aligned in a parallel manner. In quantum mechanics, if the two Fe sites have spin

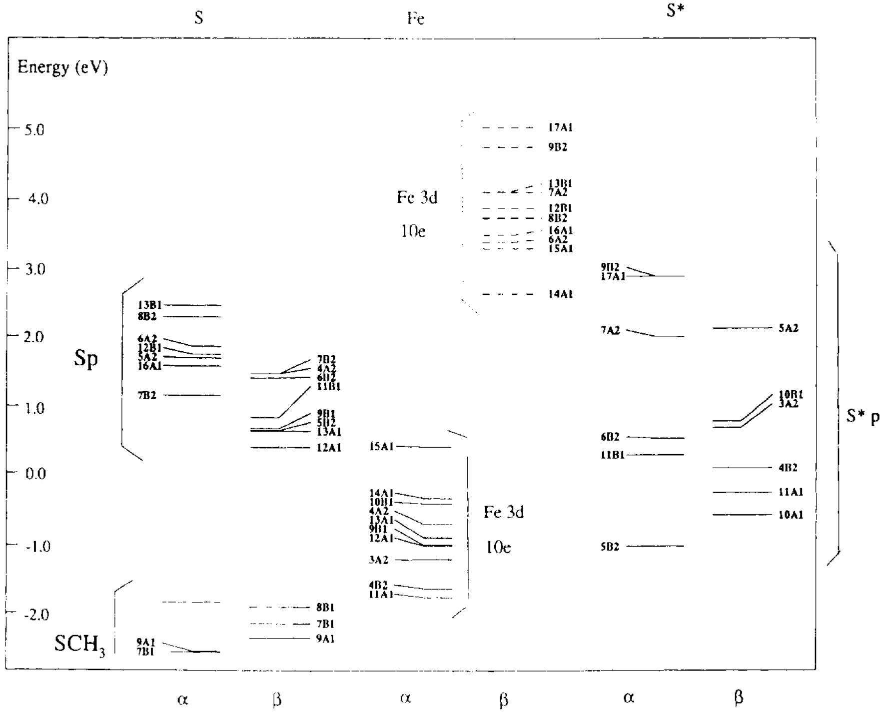

Fig. 4. Energy level diagram for the high-spin (HS) state of $[Fe_2S_2(SCH_3)_4]^{2-}$, as calculated with a density functional Vosko–Becke–Perdew (VBP) potential. Spin indices as in Fig. 2. The orbitals are separated horizontally according to their location on terminal $(SR)_2$, Fe_2 or bridging $(S^*)_2$ (left, center, right). The ten empty Fe(3d) levels (ligand field levels) are given by broken lines, while the filled Fe(3d) majority spin levels are given by full lines, along with filled S*,S(3p) levels of both spins.

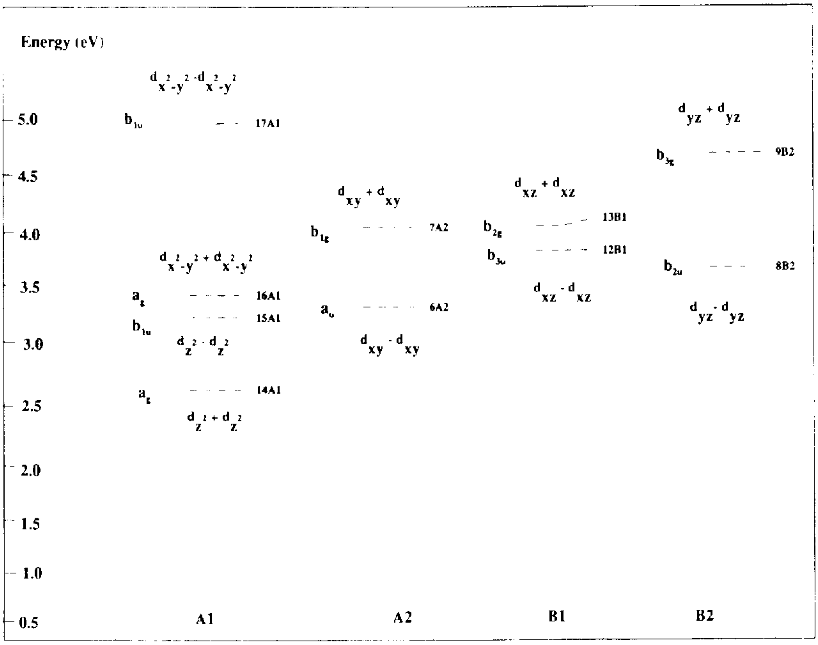

Fig. 5. The ten empty ligand field levels of the high-spin $[Fe_2S_2(SR)_4]^{2-}$ system shown on an expanded energy scale. The orbitals are grouped according to their symmetry representations in the C_{2v} point group. The detailed Fe orbital character and representations in the higher D_{2h} group are shown. Note the Fe—Fe bonding–antibonding splittings, particularly between $d_{z^2}+d_{z^2}$, $d_{z^2}-d_{z^2}$.

quantum numbers S_A and S_B, then possible spin states for the coupled system have total spin S_t ranging from $|S_A - S_B|$ to $S_A + S_B$ in integer steps, forming a ladder of pure spin states. When the fundamental electronic interactions are such that the system obeys a Heisenberg hamiltonian defined by $H_{\text{spin}} = JS_A \cdot S_B$, the successive spin state energies are given by $E(S_t) - E(S_t - 1) = JS_t$. A necessary condition for this hamiltonian is that the metal sites interact fairly weakly (per electron pair) compared with a metal–metal bond. We have presented elsewhere a perturbation theory rationalization for using a Heisenberg spin hamiltonian to describe these systems [55,56,86,91]. From the discussion above, it is evident that there are many pure spin states, but the dimer has only one broken symmetry state. It can be shown that the broken symmetry state Ψ_B is a weighted average of the pure spin states $\Psi(S_t)$, the weights being Clebsch–Gordan coefficients $(C_1(S_t) = C(S_A S_B S_t; M_{SA} M_{SB}))$, and that the broken symmetry state energy is a weighted average of the pure spin state energies [86]

$$\Psi_B = \sum_{S_t} C_1(S_t)\Psi(S_t) \qquad (1)$$

$$E_B = \sum_{S_t} C_1(S_t)^2 E(S_t) \qquad (2)$$

Since the Heisenberg spin ladder is determined by only one parameter, the energy difference between the high-spin and broken symmetry states can be used to calculated J from the equation

$$E(S_{\max}=S_A+S_B)-E_B(M_S=|S_A-S_B|)=2JS_AS_B \tag{3}$$

and the entire Heisenberg ladder of pure spin states can be constructed. This general idea also applies to Heisenberg Fe—Fe pair interactions in polynuclear complexes. A detailed exposition of its application to 3Fe systems where all the irons are in the Fe^{3+} state is given in Ref. [92]. Applications to reduced 3Fe systems are described in Ref. [93], and an initial examination of Zn3Fe systems is given in Ref. [94]. In the dimer case, there is only one broken symmetry state, but for polynuclear systems, there can be more than one. The lowest energy broken symmetry state is the one whose spin coupling pattern most resembles that in the spin ground state.

For a mixed valence Fe^{2+}–Fe^{3+} dimer, an additional complication arises. When one electron is added to the oxidized system to form a mixed valence state, the electron becomes trapped in BS, but fully delocalized in HS. This is shown schematically in Fig. 6. Because of the energetic degeneracy between the Fe^{2+}–Fe^{3+} and Fe^{3+}–Fe^{2+} configurations, resonance delocalization can occur, and the delocalization energy depends on the spin quantum number (S_{ij}) of the mixed valence pair, so that the expected spin dependence can be written as $B(S_{ij}+1/2)$, and then the delocalization energy increases with the pair spin. This resonance delocalization or double exchange hamiltonian for mixed valence pairs was first proposed by Anderson and Hasegawa [95] following the initial work of Zener [96] on mixed valence pairs. Later developments in this area, with particular reference to dinuclear and polynuclear FeS complexes, have been described in papers by Noodleman and Baerends [56], Girerd and Blondin [24,97] and Papaefthymiou et al. [98]. In the reduced

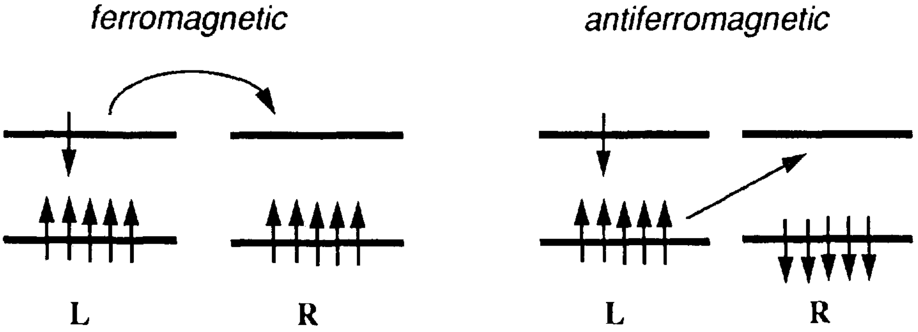

Fig. 6. Schematic diagram of the dependence of the delocalization of the sixth d electron (minority spin) on an Fe site for ferromagnetic vs. antiferromagnetic alignment of the site spin vectors. There is no barrier to resonance electron delocalization for the ferromagnetic (high-spin) alignment. By contrast, resonance delocalization of the sixth (minority spin, β, left) electron is not allowed in the broken symmetry, antiferromagnetically aligned state due to the Pauli principle (β spin orbitals are all filled on the right). Instead, some transfer of the majority spin (α, left) electrons occurs to the right, and for majority spin (β, right) to the left, but this costs energy; these terms contribute to the Heisenberg coupling in the broken symmetry state. (Reprinted with permission from Ref. [55]. Copyright, Academic Press, 1992.)

high-spin state, the bonding (g)–antibonding (u) energy splitting ($E_u - E_g$) of the minority spin Fe(3d) orbital delocalized over the Fe–Fe pair gives the B parameter, since $(E_u - E_g) = 10B$ with $S_{AB} = 9/2$. This orbital is occupied by one electron, with $\phi_g = Fe_1(d_{z^2}) + Fe_2(d_{z^2})$ and $\phi_u = Fe_1(d_{z^2}) - Fe_2(d_{z^2})$. The total Heisenberg plus resonance energy takes the form

$$E(S)_{u,g} = J_{red}S(S+1)/2 \pm B(S+1/2) \tag{4}$$

In 2Fe2S systems, valence delocalization competes directly with Heisenberg (antiferromagnetic) coupling. Heisenberg coupling usually dominates, keeping the total spin low ($S = 1/2$). While all spin states would be delocalized from the spin hamiltonian above, clearly the resonance term is smallest for $S = 1/2$ compared with larger S. We have evaluated B quantitatively by density functional methods, and obtained B in the range 400–500 cm^{-1} in reduced $Fe_2S_2(SR)_4{}^{3-}$ ($R \equiv H$ or CH_3). With B this small, we can expect asymmetric effects, including vibronic interactions, solvation and/or protein electrostatic effects, to quench valence delocalization for $S = 1/2$ [56,97]. For larger pair spins, trapping forces may be insufficient to overcome valence delocalization effects [99], as discussed below.

The broken symmetry state contains a substantial part of the antiferromagnetic coupling interaction present in the spin ground state. It is also valuable to have a reference state where the spin coupling interaction has been averaged out. We call this the spin barycenter state, and it is analogous to the barycenter state of ligand field stabilization energy, but now applied to spin coupling hamiltonians. This energy is defined by

$$E_{BAR} = \sum_S D(S)E(S) \Big/ \sum_S D(S) \tag{5}$$

where $D(S) = (2S+1)$ is the spin degeneracy of spin state S.

Figs. 7 and 8 give spin ladder diagrams for oxidized and reduced $Fe_2S_2(SR)_4{}^{2-,3-}$. For the oxidized cluster, Fig. 7 compares the simple Heisenberg spin ladder (middle) with the spin barycenter (left) and broken symmetry and high-spin calculations (right). The broken symmetry state lies above $E(S = 0)$, but well below the energy of the "uncoupled" spin barycenter state. For the reduced form, Fig. 8 shows the Heisenberg spin ladder (second column) and the Heisenberg plus resonance splitting ladder (third column). Again, the spin barycenter (first column, left) state lies well above the broken symmetry state, and both of these are above the ground state $E(S = 1/2)$. At the right, the broken symmetry (BS) energy is compared with the high-spin (HS) ($S = 9/2$) state energies. To calculate the Heisenberg parameter (J_{red}), we take the average $E(S = 9/2)$ energy; the B parameter is calculated from the ($E_u - E_g$) difference.

3.2. Hyperfine tensors and g tensors

Through the use of the Wigner–Eckart theorem and the vector model [22,100–102], we can relate the observed hyperfine parameters to intrinsic site values

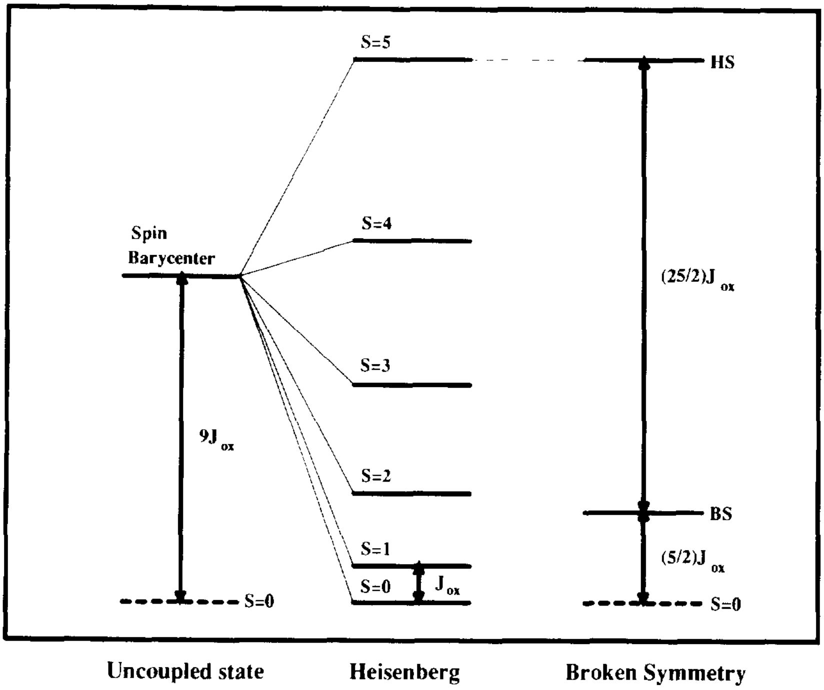

Fig. 7. The Heisenberg spin ladder for an oxidized 2Fe2S system is shown (center), along with the broken symmetry vs. high-spin energy difference used to calculate the Heisenberg coupling parameter J_{ox} (right). The spin barycenter energy is shown (left); the energy of this "uncoupled" state is compared with the ground state ($S=0$) energy. The broken symmetry state also lies above the $S=0$ ground state, but well below the spin barycenter state. All spin ladder diagrams for 2Fe2S and 4Fe4S complexes show energies to scale based on quantitative calculations of J, B and B' parameters with a VS + B potential.

a_i (characteristic of the monomer subunits). Furthermore, the total g tensor is given as a weighted sum of site g_i tensors. The lowest energy broken symmetry state provides [55,103] a direct way of evaluating intrinsic site hyperfine tensors (a_i) and site g_i tensors, which are then related to the observed A_i and total g tensor by

$$A_i = K_i \boldsymbol{a}_i \quad \text{and} \quad g_{\mathrm{tot}} = \sum_i K_i g_i \tag{6}$$

K_i are the spin projection coefficients giving the projection of the local site spin S_i onto the total spin S_{t}

$$K_i = \langle S_{iz} \rangle / \langle S_{\mathrm{t}z} \rangle = \langle \boldsymbol{S}_i \cdot \boldsymbol{S}_t \rangle / \langle \boldsymbol{S}_t \cdot \boldsymbol{S}_t \rangle \tag{7}$$

This equation has a simple closed form when the total spin vector of the system $\boldsymbol{S}_t = \boldsymbol{S}_i + \boldsymbol{S}_j$ and S_i, S_j and S_{t} are good spin quantum numbers

$$K_i = [S_{\mathrm{t}}(S_{\mathrm{t}}+1) + S_i(S_i+1) - S_j(S_j+1)] / [2S_{\mathrm{t}}(S_{\mathrm{t}}+1)] \tag{8}$$

For dimer systems, Eq. (8) can be used directly giving $K_1 = 7/3$ and $K_2 = -4/3$ for

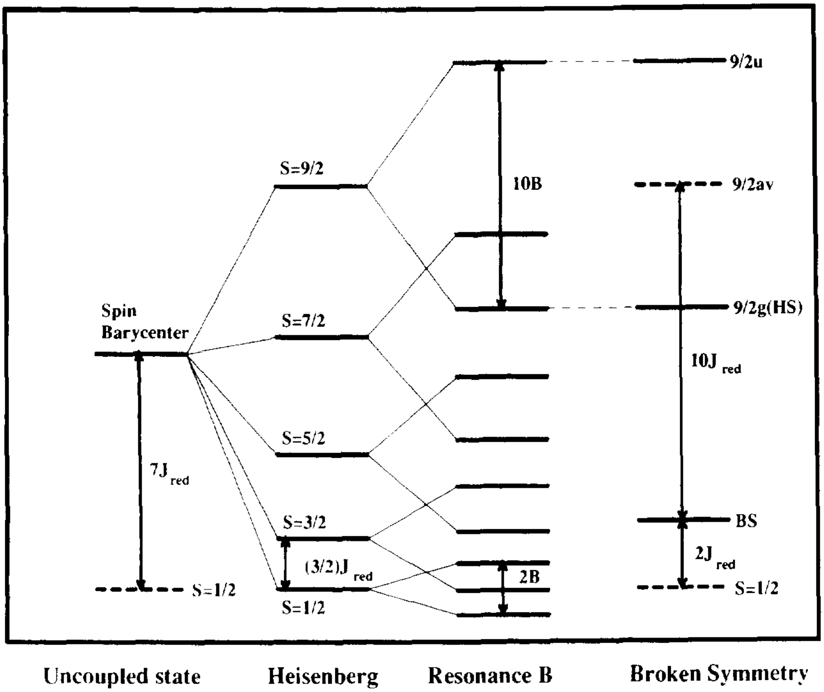

Fig. 8. The spin hamiltonian energies for a 2Fe2S reduced system. Starting from the left, the energies of the spin barycenter ("uncoupled") state, the Heisenberg spin ladder and the Heisenberg plus resonance splitting energies are shown. At the right, the broken symmetry (BS) energy is shown in comparison with the high-spin (HS) $S=9/2$ energies for the bonding (g), antibonding (u) and average (av) states. The Heisenberg parameter (J_{red}) is determined from the difference energy $10J_{\text{red}}$ as indicated (right), while the resonance (B) parameter is calculated from the HS ($E_u - E_g$) ($S=9/2$) energy difference $10B$. (Reprinted with permission from Ref. [70]. Copyright, American Chemical Society, 1994.)

the ferric and ferrous sites respectively in the $S_t = 1/2$ ground state [100,104]. For polynuclear systems (for example, in 4Fe4S systems), completely analogous equations can be used to obtain the spin projection coefficient for coupling the sites S_i, S_j to an intermediate spin S_q, and then for coupling the subunits S_q ($q = 1, 2$) to the total spin S_t (by replacing the spins S_i, S_j by S_q).

Another necessary condition for application of the above equations is that the relevant Heisenberg J parameters must be much greater than site zero field splitting (ZFS) parameters, which is a good approximation for most FeS complexes, with small correction terms when $S_t = 1/2$ [105,106]. Site and net system zero field splittings can significantly affect spin-dependent properties when $S_t > 1/2$. Both the effective g values and the internal magnetic fields are strongly affected. For large total spin, the internal magnetic fields are often uniaxial, with the main axis determined by the largest principal value of the ZFS tensor. These effects can considerably complicate the observed spectrum, but are beyond the scope of this review.

3.3. Spin projection chain and sum rules

Next, we introduce the spin projection chain rule for a total system spin composed of subunits with good spin quantum numbers. Let us consider a system of total spin S_t, which can be decomposed into two subunits of spin S_q which couple together to give S_t, and where each subunit can in turn be decomposed into a sum of site spins S_i. Then, the spin projection coefficient K_i^q for projecting the local site spin S_i onto the subunit spin S_q is

$$K_i^q = \langle S_{iz} \rangle / \langle S_{qz} \rangle \tag{9}$$

Similarly, the coefficient for projecting the subunit spin S_q onto the total system spin S_t is

$$K_q^t = \langle S_{qz} \rangle / \langle S_{tz} \rangle \tag{10}$$

Then, the spin projection coefficient for projecting the site spin onto the total system spin is

$$K_i = [\langle S_{iz} \rangle / \langle S_{qz} \rangle][\langle S_{qz} \rangle / \langle S_{tz} \rangle] = K_i^q K_q^t \tag{11}$$

This equation is very useful when obtaining spin projection coefficients for 4Fe complexes from those of dimeric subunits [74,107,108]; it is also applicable to the P clusters of nitrogenase containing an 8Fe cluster [109]. In the latter, the hyperfine parameters of the sites in the complete system can be related to those expected for 4Fe subunits, using the hyperfine parameters of typical 4Fe4S and 4Fe4Se systems. Alternatively, from intrinsic site hyperfine parameters (a_i), the parameters for the complete 8Fe complex can be predicted for various postulated spin coupled states by successively coupling together individual site spins, to pairs, to cubane subunits and then to the total cluster spin.

There is also a sum rule that applies to the spin projection coefficients

$$\sum_i K_i = \sum_i \langle \boldsymbol{S}_t \cdot \boldsymbol{S}_i \rangle / \langle \boldsymbol{S}_t \cdot \boldsymbol{S}_t \rangle = 1 \tag{12}$$

This result is well known for spin coupled dimers [22], trimers [110] and tetramers [111]. It is applicable generally, and has been used recently for mixed metal MFe_3 complexes [112]. It has considerable value for analysis where some K_i values of a cluster can be determined accurately, while others are ill-determined or are unknown.

4. Applications to cubane-like iron–sulfur clusters

4.1. Overview

The 2Fe2S ferredoxins exhibit trapped Fe^{2+}–Fe^{3+} valence sites in the mixed valence state [100], whereas Mössbauer spectroscopy shows that 4Fe4S clusters exhibit delocalized valence electron distributions over specific $Fe^{2.5+}$–$Fe^{2.5+}$ dimers [74,75,113]. Our work [55] and that of others [24,114,115] has shown that the spin state of a system is often the result of competition between Heisenberg exchange and resonance delocalization (double exchange). Since there are many possible spin quantum states that can differ not only in total spin, but also in intermediate spin, we need to understand what electronic effects are decisive in selecting out the spin coupling pattern of the ground state and low-lying excited states, and how this is related to electron delocalization.

A Heisenberg-only hamiltonian for a 4Fe4S system with a single J parameter has a highly degenerate spin ground state, with many possible spin alignments for each Fe–Fe dimeric subunit, but this is inconsistent with the magnetic hyperfine parameters observed by Mössbauer spectroscopy for the spin ground states of the odd-electron systems. It is generally observed that only a few particular spin alignment patterns are found for the dimeric subunits. However, these can still generate a considerable variety of final spin states. Furthermore, Mössbauer spectroscopy, which allows the cross-correlation of isomer shifts, quadrupole splittings and magnetic hyperfine parameters for Fe sites, shows that delocalized, mixed valence pairs have parallel or nearly parallel Fe spin vectors. This correlation of spin alignment and electron delocalization does not occur within a spin hamiltonian with only Heisenberg-type coupling terms, even where multiple J parameters are postulated.

As discussed above, the addition of resonance delocalization terms of the form $B(S_{ij}+1/2)$ dramatically changes this situation, and the overall spin state now represents a compromise between these competing forces. The concept of "spin frustration" is well known in polynuclear transition metal complexes; antiferromagnetic coupling (governed by one or more J parameters) cannot lead to antiparallel alignment of all metal–metal spin pairs, because the various metal sites are interconnected in globular clusters [25]. Spin frustration also occurs in systems where both Heisenberg antiferromagnetic coupling and resonance delocalization are simultaneously present, but here the resonance terms will help to determine the lowest energy spin states, as shown by the following simple argument. In mixed valence complexes with substantial orbital overlap, the resonance delocalization (double exchange) energy of a pair is largest for parallel spins. Consequently, for the lowest energy states, in 3Fe, 4Fe and MFe_3 systems, some pair spin vectors can be large, facilitating valence delocalization, while keeping many other pair spin vectors small (with antiparallel alignment of the corresponding site spins), maintaining a favorable Heisenberg antiferromagnetic energy.

Some simple examples of this correlation of spin states and electron delocalization are apparent in Fe_3S_4 and MFe_3S_4 systems [116,117]. In $[Fe_3S_4]^0$, the total spin $S_t=2$, and this cluster appears to be composed of a delocalized $Fe^{2.5+}$–$Fe^{2.5+}$ pair with spin $S_{12}=9/2$ antiferromagnetically coupled to an Fe^{3+} site with $S_3=5/2$. The $[ZnFe_3S_4]^+$ system has total spin $S_t=5/2$, and is composed of a similar delocalized $S_{12}=9/2$ pair antiferromagnetically coupled to an Fe^{2+} site with $S_3=2$. Similarly, a delocalized $S_{12}=9/2$ pair is coupled to a parallel aligned $Fe^{2+}(S_3=2)$–$Ni^{2+}(S_4=1)$ pair to give the net spin of $S_t=3/2$. Thus the $S_{ij}=9/2$ delocalized pair appears to be a typical subunit in these systems. Despite this apparent simplicity, there are a number of subtle issues involved in the electronic structure of 3Fe and MFe_3 mixed metal complexes with respect to magnetic properties, and concerning the electronic and spin interactions of the heterometal site with the iron sites, but the basic spin coupling appears to be well understood.

This general picture also applies to cubane-like 4Fe4S and 4Fe4Se systems. In $[Fe_4S_4]^{2+}$, there are two parallel Fe–Fe pair spin vectors, and four antiparallel, and, correspondingly, two delocalized $Fe^{2.5+}$–$Fe^{2.5+}$ pairs, each associated with a parallel spin Fe–Fe pair (see Fig. 1). The antiferromagnetic coupling of these two pairs yields a total spin $S_t = 0$. Adding or subtracting one electron can yield a variety of spin and electronic states, and this has a profound effect on the observed properties. For example, in 4Fe4S cluster states 3+ and 2+, the ground spin states (with $S = 1/2$ and $S = 0$ respectively) are well separated in energy from states of higher spin. In contrast, the 1+ oxidation state may have ground states with $S = 1/2$, 3/2 and 7/2 or statistical mixtures of these in different proteins or synthetic analogs, and excited spin states appear at lower energy than in the 3+ or 2+ oxidation states. Both experimental studies of the magnetic susceptibility and recent theoretical analyses show that there is a significant decrease in the size of the Heisenberg antiferromagnetic coupling constants J when the cluster oxidation state is reduced from 3+ to 2+ to 1+. The different spin states and patterns of electron delocalization and spin coupling serve as important probes of the differences among proteins and clusters.

We have already noted the importance of resonance delocalization over particular mixed valence pairs; there are two such pairs for the 2+ oxidation form and one pair for either the 3+ or 1+ oxidation state. The resonance stabilization energy of each pair is $B(S_{ij} + 1/2)$, where S_{ij} is the spin of the pair. It is also possible to have delocalization between the ferric and mixed valence pairs in the 3+ cluster, and between mixed valence and ferrous pairs for the 1+ state. The corresponding resonance term, now representing a resonance over the entire cluster (all Fe sites) is $B'(S_t + 1/2)$, where S_t is the total system spin. Here, S_t acts like the total pair spin of the reduced 2Fe2S system, and the pair spins themselves (S_{12}, S_{34}) are analogous to the individual site spins of the reduced 2Fe2S system, using a Heisenberg plus resonance hamiltonian, as in Fig. 8.

In the following sections, we consider in turn the orbital and spin coupling aspects of the 4Fe4S complexes. Initially, the broken symmetry and pure spin states are considered in the framework of spin hamiltonians of rather high symmetry, having a single Heisenberg J coupling parameter and resonance parameters B, B'. These parameters can be determined from energy differences between the high-spin and broken symmetry states, along with energy differences for electronic excitations within these states (the B parameter from the intralayer $g \rightarrow u$ energy difference within the broken symmetry state, and the B' parameter from the interlayer resonance energy of the high-spin state). The consequences of these spin hamiltonians are then explored. Subsequently, we extend these spin hamiltonians to allow for two different J parameters in the $HP_{ox}(3+)$ and $Fd_{red}(1+)$ type systems. We then explore the relationship between these spin hamiltonians and the properties of experimentally characterized systems.

4.2. Orbital states of 4Fe4S complexes

Fig. 1 shows schematically how the two minority spin electrons, one for each $Fe_2S_2^*(SR)_2$ layer, are delocalized across opposite cube faces in the $[Fe_4S_4]^{2+}$ oxidation state. In orbital terms, these are $20a_1\alpha, \beta$ of the broken symmetry state (the point group of the electronic hamiltonian is C_{2v}, while the geometric group is D_{2d}).

For further analysis, the two layers can be labelled t for top and b for bottom. Let the two Fe–Fe pairs be Fe_t–Fe_t (x axis) and Fe_b–Fe_b (y axis), with z perpendicular to these, corresponding to the axis of compression of the cluster. A color 3-D isovalue map of the minority spin $20a_1\beta$ orbital (Fe–Fe σ bonding $Fe_{t1}(d_{x^2-y^2}) + Fe_{t2}(d_{x^2-y^2})$) from the broken symmetry state is shown in Ref. [55].

The corresponding $20a_1\alpha$ orbital is related by an S_4 symmetry operation (about the z axis) of the D_{2d} geometric point group acting on $20a_1\beta$ combined with spin reversal (transforming the Fe–Fe pair (top) into the Fe–Fe pair (bottom)) and conversely. Similarly, the large spin vectors and their corresponding spin orbitals can be interconverted under this operation of the D_{2d} group, combined with spin reversal. We have here the molecular analog of the color (Shubnikov) groups from the solid state theory of magnetic crystal lattices [118].

As in the 2Fe2S case, the mainly Fe(3d) majority spin orbitals are low lying. The overall level structure of the $[Fe_4S_4]^{2+}$ oxidation state (broken symmetry state) has been depicted previously, from Xα-scattered wave calculations [67]. Both Xα-LCAO (linear combination of atomic orbitals) calculations and VS + B (Vosko–Stoll potential plus Becke exchange energy correction) calculations give a qualitatively similar picture for the overall level structure for both the majority spin and minority spin orbitals [42,55].

Fig. 9 shows the energies of the two highest occupied majority spin orbitals for each layer and the single highest occupied minority spin orbital ($20a_1\beta$ for the top layer; $20\alpha_1\alpha$ for the bottom layer), together with the lowest lying empty levels. The two highest occupied majority spin orbitals ($14b_1\alpha$, $13b_2\alpha$ top) are largely from the exchange split S,S*(3p) band of levels, but with significant Fe(3d) mixing. These will prove important when we consider the low-lying orbital electronic states of the 3+ cluster form, HP_{ox}.

The S_4 operation of D_{2d} transforms $b_1 \leftrightarrow b_2$, which accounts for the energetic degeneracy of $b_1\alpha$ in one layer with $b_2\beta$ in the opposite layer. Similarly, there is energetic degeneracy beween $b_2\alpha$ and $b_1\beta$ in the opposite layer. In the correlation table of the D_{2d} point group with the C_{2v} subgroup, the degenerate representation $e \rightarrow b_1 + b_2$, and b_1 and b_2 are orthogonal components [119].

Focusing now on the empty levels in the top layer, β spin, we find that they are of two kinds. The $9a_2$ level is of δ* character with respect to the Fe–Fe interaction $Fe_{t1}(d_{yz})$–$Fe_{t2}(d_{yz})$ (perpendicular to the Fe_t–Fe_t x axis), while $14b_1$ is the σ* antibonding counterpart to $20a_1$. The resonance delocalization parameter within either of the two mixed valence pairs can be calculated from $10B = \Delta E(14b_1 - 20a_1)$, where ΔE is the excitation energy for this transition and $10B$ is the double exchange form

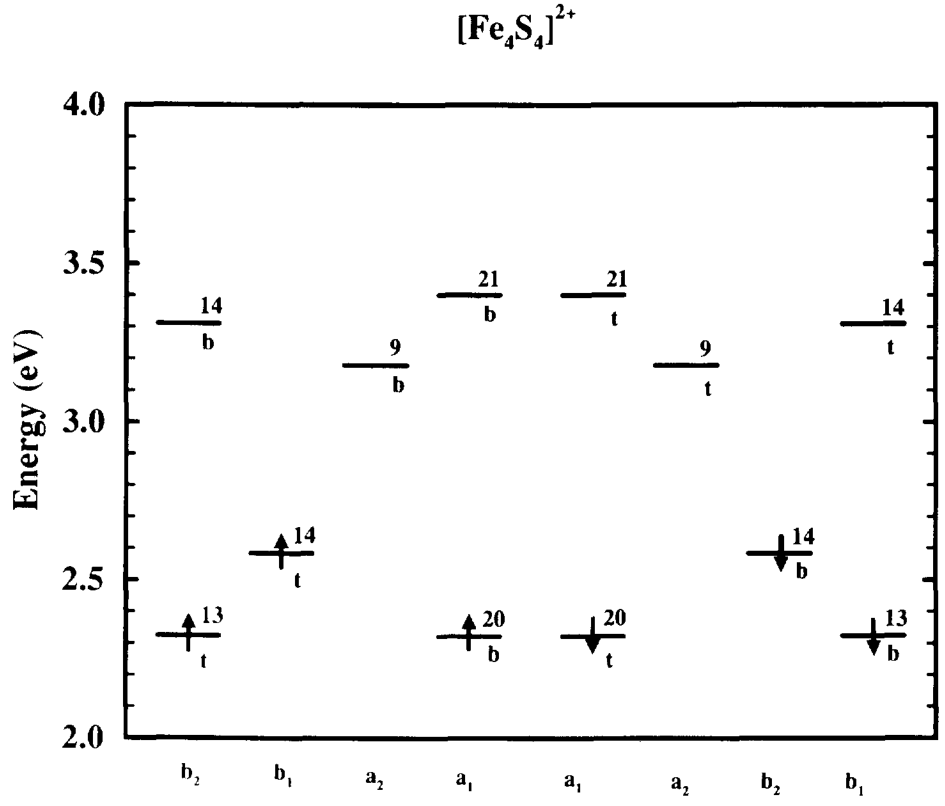

Fig. 9. The highest occupied and lowest unoccupied levels are shown for $[Fe_4S_4(SCH_3)_4]^{2-}$, as calculated with a VS + B potential. The oxidation state is equivalent to ferrodoxin (oxidized) and to HIPIP (reduced). The symmetry labels in C_{2v} electronic symmetry are given on the horizontal axis. In the diagram, t = top and b = bottom of the molecule, the numbering of the energy levels is given for each symmetry and the occupied levels are shown with up-spin arrow for α and down-spin for β.

of the resonance splitting energy $2B(S_{ij}+1/2)$, where $S_{ij}=9/2$ for the parallel spin alignment within the mixed valence pair.

The electronic character of the reduced 1+ cluster form (Fd_{red}) depends on whether $14b_1$ or $9a_2$ is occupied, and these lie very close in energy. Fig. 10 shows the orbital level diagram resulting from the occupation of $14b_1\beta$. We will refer to this state as OC1 (orbital configuration 1). We also show how the alternative orbital configuration OC2 (orbital configuration 2) can be obtained by a spin allowed transition $14b_1 \rightarrow 9a_2$, or $\sigma^* \rightarrow \delta^*$. The major difference here is in the occupation scheme of the ferrous layer (Fe^{2+}–Fe^{2+}), which changes from ($20a_1, 14b_1$) to ($20a_1, 9a_2$), β spin, while the mixed valence pair retains the occupied $20a_1\alpha$ orbital, giving resonance delocalization within this layer. The consequences of this for spin states are discussed below.

For the $[Fe_4S_4]^{3+}$ HP_{ox} system, there are three low-lying electronic states from

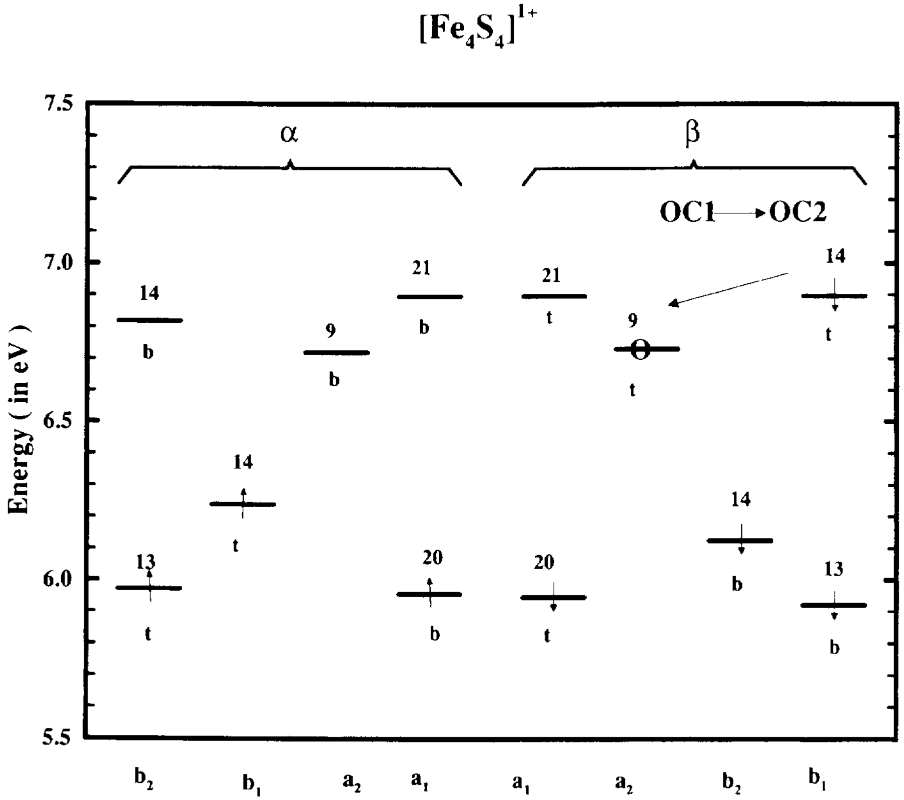

Fig. 10. The highest occupied and lowest unoccupied levels are shown for $[Fe_4S_4(SCH_3)_4]^{3-}$, as calculated with a VS + B potential. The electronic configuration is OC1 (orbital configuration 1), and the transition to OC2 (orbital configuration 2) is shown (see the hole in $9a_2\beta$). The α and β levels are shown by braces, and the occupied levels are indicated with arrows. (Redrawn from Ref. [70]. Copyright, American Chemical Society, 1994.)

the broken symmetry calculations, obtained by removing one electron from the 2+ cluster; these three states, designated OS1, OS2 and OS3 (OS, orbital state), differ mainly in the nature of the Fe^{3+}–Fe^{3+} pair, with the delocalized mixed valence pair being quite similar in all states. The energy level diagrams are given in Fig. 11. The hole is in $20a_1\beta$ for OS3, and this moves to $14b_1\alpha$ for OS1, or to $13b_2\alpha$ for OS2. The sites of the diferric pair are both high-spin $S_i = 5/2$ for state OS3, but these are a quantum mixture of high-spin and intermediate spin $S_i = 5/2$, 3/2 for OS1 and OS2. (The situation may be something like the spin state of ferric iron in some heme complexes, which are $S = 5/2$ or 3/2, or mixtures thereof [120].)

Now let us consider the orbital interactions which are important for determining the resonance interaction between a mixed valence pair and a ferric pair (3+, HP_{ox}) or between a mixed valence pair and a ferrous pair (1+, Fd_{red}). These are interlayer interactions. They are mostly absent in the broken symmetry state, since the spin

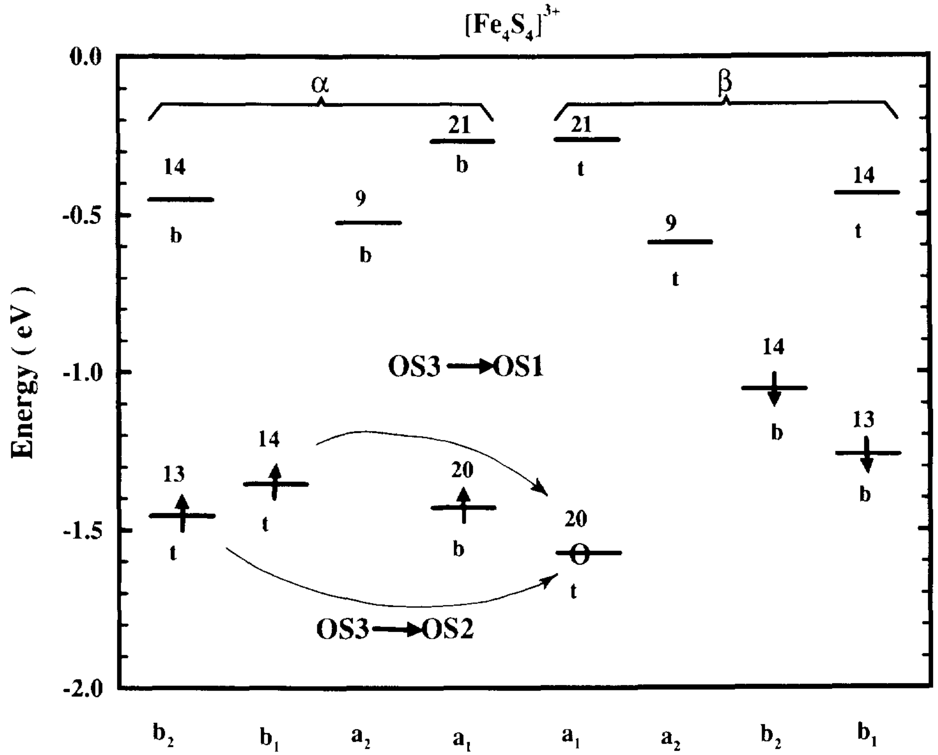

Fig. 11. The highest occupied and lowest unoccupied levels are shown for $[Fe_4S_4(SCH_3)_4]^{1-}$, with the VS + B potential, as in HP_{ox}. The orbital electronic state given in OS3, and the excitations which give OS1 and OS2 are shown. Notice that these are spin forbidden transitions, from occupied α spin orbitals to the empty $20a_1\beta$ hole. (Redrawn from Ref. [70]. Copyright, American Chemical Society, 1994.)

vectors of the two layers are oppositely aligned, but are fully present in the high-spin states, with all Fe spin vectors parallel aligned ($S_t = 19/2$ (or 17/2) for HP_{ox} and $S_t = 17/2$ for Fd_{red}). We consider a molecular geometry with D_{2d} symmetry; the high-spin states then have D_{2d} for the electronic symmetry. The resonance delocalization of an orbital depends strongly on its symmetry in the D_{2d} group and C_{2v} subgroup; only energetically degenerate levels from the different $Fe_2S_2^*(SR)_2$ layers can be combined. Starting with the C_{2v} group, orbitals of a_1 character can combine to give cluster orbitals a_1, b_2 in D_{2d}; $a_2(C_{2v})$ gives a_2, $b_1(D_{2d})$, while b_1, $b_2(C_{2v})$ are components of e in D_{2d} [119]. This implies that of the C_{2v} layer orbitals, a_1 and a_2 give net interlayer resonance $B' \neq 0$, because the orbitals of different symmetry in D_{2d} will also have different energies, while b_1, b_2 give $B' = 0$, because of the twofold degeneracy of the e representation.

4.3. Spin states of 4Fe4S complexes

Fig. 12 shows the Heisenberg and Heisenberg plus resonance spin ladders for the $[Fe_4S_4]^{2+}$ cluster form, equivalent to HP_{red} and to Fd_{ox}. The corresponding spin

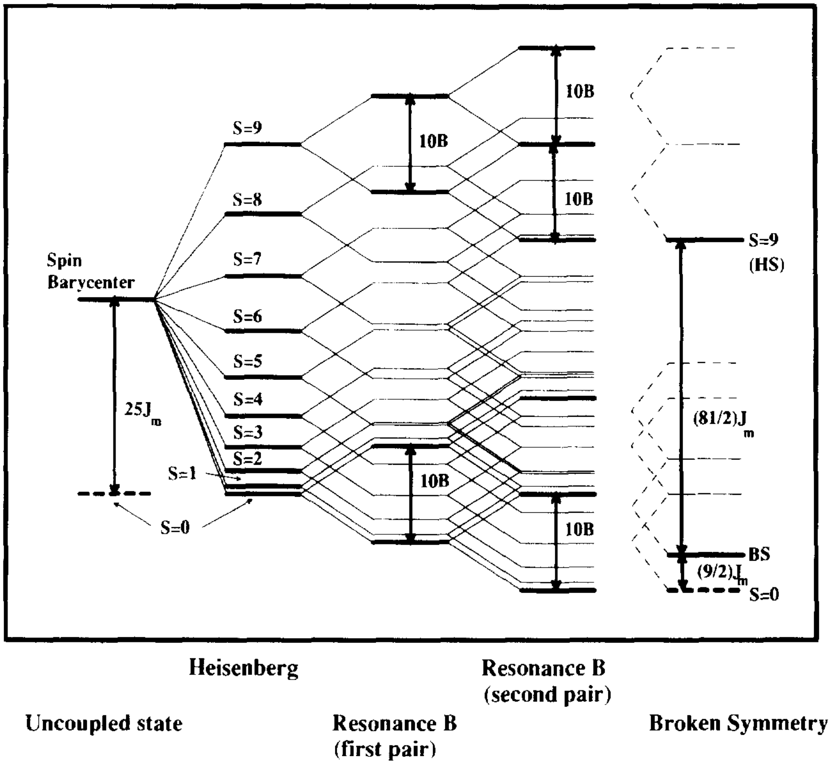

Fig. 12. Spin state diagram for $[Fe_4S_4(SR)_4]^{2-}$, as in Fig. 9. The position of the spin barycenter state, the Heisenberg (only) spin ladder and the successive addition of the first and second resonance pair interactions are shown. For clarity, only the $S_{12} = S_{34} = 9/2$ (maximum pair spin states) are shown. The broken symmetry (BS) energy is compared with that of the high-spin state (HS, $S = 9$) and the spin ground state energy ($S = 0$). The Heisenberg parameter J_m is calculated from the HS minus BS energy difference, while the resonance splitting parameter B is calculated from the $E_u - E_g = 10B$ difference in the BS state. All energies are to scale based on the calculations.

hamiltonian is

$$H = J_m \sum_{i<j=1,4} S_i \cdot S_j \pm B(S_{12} + 1/2) \pm B(S_{34} + 1/2) \tag{13}$$

with energies

$$E(S) = (J_m/2)S(S+1) \pm B(S_{12} + 1/2) \pm B(S_{34} + 1/2) \tag{14}$$

where $S = S_t$, the total system spin. The resonance terms, giving the spin-dependent delocalization energy, can be derived in a more general way from a spin-dependent transfer operator BT_{ij} which generates the appropriate Racah coefficient [24,98].

The range of S_{12}, S_{34} is given by the vector sum formula (also called the triangle inequality)

$$|S_1 - S_2| \leqslant S_{12} \leqslant S_1 + S_2 \tag{15}$$

or $1/2 \leqslant S_{12} \leqslant 9/2$, with a similar equation for S_{34}. Also, the range of total S allowed is

$$|S_{12} - S_{34}| \leqslant S \leqslant S_{12} + S_{34} \tag{16}$$

The resonance part of the diagram is actually simplified by showing only those states derived from $S_{12} = S_{34} = 9/2$ (maximum values). These pair quantum numbers are characteristic of the broken symmetry state (shown on the right), the spin $S = 0$ ground state (also shown on the right, and as the lowest thick line in the fourth column) and the highest spin state $S = 9$. The spin barycenter state, where both Heisenberg coupling and resonance delocalization are averaged out, is shown in the leftmost column. (The spin barycenter is calculated for the maximum fixed pair spins $S_{12} = S_{34} = 9/2$, since these apply to the spin ground state as well as to the broken symmetry state.) The second column contains the Heisenberg ladder alone (with B terms averaged out). On the right (labelled broken symmetry), the procedure for calculating the Heisenberg parameter J_m is illustrated

$$E(S_{\mathrm{max}}) - E_{\mathrm{B}} = 2J_m(S_{12})_{\mathrm{max}}(S_{34})_{\mathrm{max}} = 81J_m/2 \tag{17}$$

As described above, the B parameter is calculated from the g→u orbital energy difference within the broken symmetry state.

Fig. 13 shows the Heisenberg plus resonance spin ladders for reduced $[\mathrm{Fe_4S_4}]^{1+}$ clusters, equivalent to $\mathrm{Fd_{red}}$. The corresponding spin hamiltonian is

$$H = J_{\mathrm{rd}} \sum_{i<j=1,4} S_i \cdot S_j \pm B(S_{34} + 1/2) \pm B'(S + 1/2) \tag{18}$$

with solutions

$$E(S) = (J_{\mathrm{rd}}/2)S(S+1) \pm B(S_{34} + 1/2) \pm B'(S + 1/2) \tag{19}$$

where S_{34} is the mixed valence pair spin and S is the total system spin. Fig. 13 includes the location of the spin barycenter state, the Heisenberg ladder and the effects of resonance delocalization within the mixed valence pair (B term) and between mixed valence and ferrous pairs (B' term). The last column (right) shows how J_{rd} is calculated from the $E(S_{\mathrm{max}} = 17/2) - E_{\mathrm{B}}$ energy difference. The B parameter is once again obtained from the resonance splitting of the g and u energies in the mixed valence pair; the B' parameter is obtained within the high-spin ($S = 17/2$) state from the interlayer resonance splitting of $\mathrm{a_2}(C_{2v})$ (Fe–Fe δ* orbital) which generates $\mathrm{a_2}$, $\mathrm{b_1}$ in D_{2d}. The orbital configuration shown is OC2, so that $B' \neq 0$, as outlined above. The presence of a B' term allows the final spin ladder to be non-monotonic with respect to the total spin S; that is, $S = 3/2$ can lie below $S = 1/2$ if B'/J_{rd} is large enough (for $B'/J_{\mathrm{rd}} \geqslant 3/2$). By contrast, occupation of the Fe–Fe σ* orbital (with orbital symmetry $\mathrm{b_1}$ or $\mathrm{b_2}$) gives $B' = 0$, in orbital configuration OC1. Our density functional calculations, with a VS + B potential, predict that OC2 and OC1 are very close in energy, with OC2 slightly lower

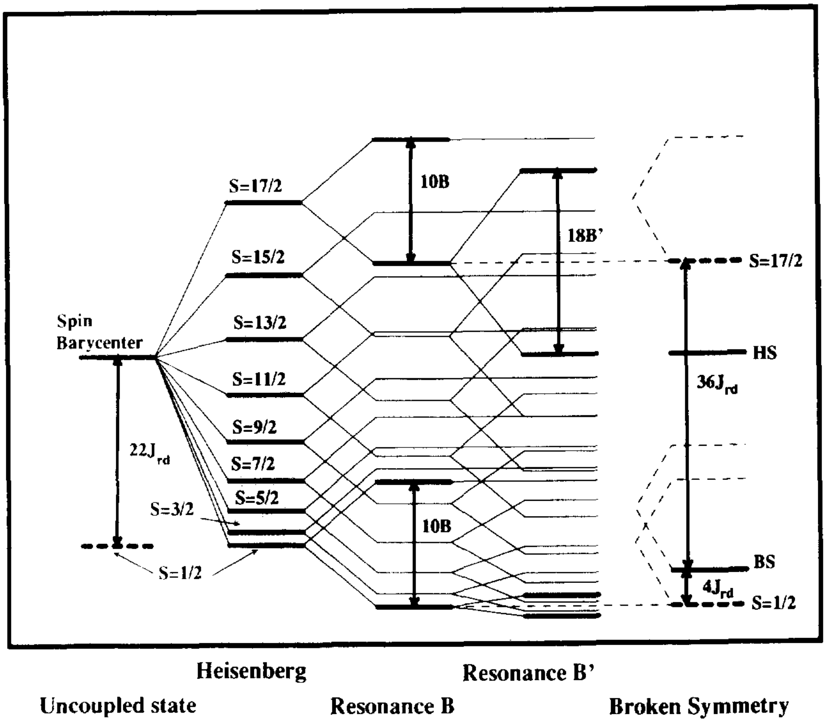

Fig. 13. Spin state diagram for $[Fe_4S_4(SR)_4]^{3-}$, for the orbital electronic state OC2 (see also Fig. 10). The spin barycenter position, Heisenberg ladder, Heisenberg plus resonance ladder (due to intralayer delocalization within the mixed valence pair), and the added effect of interlayer resonance (with parameter B') are given. When the B' term is included, the lowest energy $S = 3/2$ state is only slightly above the lowest $S = 1/2$. The positions of the BS state and HS state are shown, together with the procedure for evaluating J_{rd}, B and B' (obtained from the HS ($S = 17/2$, average) minus BS energy, from calculations of $10B$ by taking an orbital excitation energy within the BS state, and from $18B'$ by taking an energy difference within the high-spin $S = 17/2$ set of states).

in our model system (by about 0.1 eV); this is also shown in the broken symmetry level structure of Fig. 10. $B' = 0$ implies that the resonance B' splitting in Fig. 13 is absent in OC1, and $S = 1/2$ in the ground state [70].

For reduced 4Fe (Fd_{red} and synthetic analogs), there are thus two nearly degenerate electronic configurations. Either of these could represent the ground state of the system, and in low symmetry environments, these different orbital states can mix and split from theoretical considerations. Analysis of the calculations and of the corresponding spin hamiltonian then shows that one electronic configuration (OC1) must have an $S = 1/2$ ground spin state, while for the other, either $S = 1/2$ or $S = 3/2$ can be the ground state, depending on the detailed spin hamiltonian parameters (cf. Fig. 13). These predictions are in good correspondence with the observed presence of spin ground states $S = 1/2$ or $S = 3/2$ (or mixtures of $S = 1/2, 3/2$) in different reduced 4Fe4S complexes and proteins [121,122]. Also, full valence delocalization over the cluster (Robin–Day class III behavior [123]) or a small inequivalence between the mixed valence and the ferrous pairs is observed when the ground state is $S = 3/2$, and usually larger inequivalence between pairs for $S = 1/2$ (Robin–Day class III within the mixed valence pair; Robin–Day class II between the mixed valence and ferrous pairs). This is in good accord with the calculations, since resonance delocalization within the mixed valence pair is always energetically large, resonance between pairs can give either an $S = 1/2$ or $S = 3/2$ ground state, and larger delocalization (or less external trapping) favors $S = 3/2$. The Mössbauer quadrupole splitting (ΔE_Q) is typically smaller on the diferrous pair of $S = 3/2$ systems compared with $S = 1/2$, and $S = 1/2$ states have highly variable ΔE_Q [121,122]. This is consistent with the occupation of $\sigma\delta^*$ (OC2) for $S = 3/2$, since this has a lower calculated quadrupole splitting than $\sigma\sigma^*$ (OC1) [67]. These Mössbauer quadrupole splittings are consistent with OC1 and OC2, or some mixture of these for $S = 1/2$ systems.

Fig. 14 shows the Heisenberg plus resonance ladder for HP_{ox} systems (for orbital

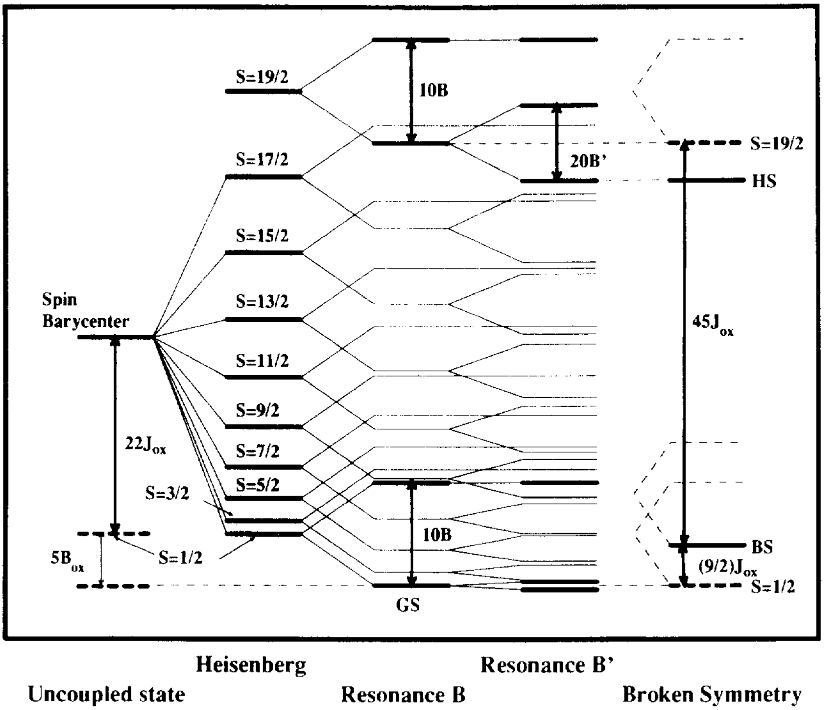

Fig. 14. Spin state diagram for $[Fe_4S_4(SR)_4]^{1-}$, for the orbital electronic state OS3 (see also Fig. 11). From left to right, the energies of the spin barycenter state, the Heisenberg spin ladder, the added effect of intralayer resonance (B term) and the additional effect of interlayer resonance (B' term) are shown. The last column shows the energy of the broken symmetry state compared with the ground state ($S = 1/2$) and the high-spin state (HS is the lowest energy high-spin state $E_g(S = 19/2)$). The Heisenberg parameter J_{ox} is obtained from the difference $E(S = 19/2)_{av(B')} - E_B$. (Reprinted with permission from Ref. [70]. Copyright, American Chemical Society, 1994.)

state OS3) corresponding to the spin hamiltonian

$$H = J_{\mathrm{ox}} \sum_{i<j=1,4} S_i \cdot S_j \pm B(S_{34} + 1/2) \pm B'(S + 1/2) \tag{20}$$

with solutions

$$E(S) = (J_{\mathrm{ox}}/2)S(S+1) \pm B(S_{34} + 1/2) \pm B'(S + 1/2) \tag{21}$$

where S_{34} is the mixed valence pair spin and S is the total system spin. Although the diferric pair spin does not appear explicitly in the energy expression, it is important because of the distinction between the orbital and spin composition of OS1 and OS2 vs. OS3. For OS3, the maximum diferric pair spin is $S_{12} = 5$, whereas for OS1 and OS2 the maximum diferric spin is only $S_{12} = 4$. The largest possible total spin is then $S = 19/2$, but only $S = 17/2$ for OS1 and OS2. The J_{ox} parameter is again determined from a comparison of the high-spin and broken symmetry energies

$$E(S_{\max})_{\mathrm{av}(B')} - E_{\mathrm{B}} = 2J_{\mathrm{ox}}(S_{12})_{\max}(S_{34})_{\max} \tag{22}$$

This energy difference is $45J_{\mathrm{ox}}$ for OS3, but only $36J_{\mathrm{ox}}$ OS1 and OS2. We note also that the $E(S_{\max}) - E(S_{\min} = 1/2)$ energy will also have a different form for OS1 and OS2 vs. OS3.

As in previous symmetry arguments, $B' \neq 0$ for OS3, and the electron in a_1 (Fe–Fe σ bonding) can delocalize with energy $B'(S + 1/2)$). (Equivalently, we can say that the hole in a_1 is delocalizing.) By contrast, in OS1 and OS2 the hole is derived from b_1 or b_2 symmetry orbitals, and $B' = 0$ by symmetry, so there is no B' term. Even for the OS3 state of $\mathrm{HP_{ox}}(3+)$, the B' term (interlayer resonance) is quantitatively smaller than for the OC2 state of $\mathrm{Fd_{red}}(1+)$ based on VS + B calculations (about half as large). This is not surprising since the δ^*–δ^* interlayer overlap in the reduced clusters is larger than the σ–σ overlap in the oxidized systems. Consistently, only $S = 1/2$ ground states have been seen in $\mathrm{HP_{ox}}$ systems, while both $S = 1/2$ and $S = 3/2$ have been observed in $\mathrm{Fd_{red}}$ systems.

The electronic structure of most HP protein active sites, judging from the observed g tensors (nearly axial with all g values above 2.0, and $g_1 > g_2 = g_3$) [75], appears closest to that expected for OS3, which we originally proposed to be the lowest lying electronic state [108]. The low-lying spin coupled states are similar for all three orbital electronic states, as in Fig. 14, based on our initial calculations of spin coupling parameters. We are in the process of examining the properties of the three different orbital electronic states for comparison with HP proteins and synthetic analogs. The synthetic analogs, in particular, show considerable variability and sensitivity in experimental g tensors [75], and this requires further study.

4.4. *Redox potentials*

Since electron transfer plays a key role in the function of many iron–sulfur clusters, it is clearly of great interest to understand the ways in which electron delocalization and spin coupling affect redox potentials. Until recently, realistic calculations of redox potentials were not feasible for two reasons. First, even for the hypothetical gas phase clusters, the electron affinities or ionization potentials computed from early quantum mechanical methods were unreliable. Second, no generally applicable theory for solvent or environmental effects was available that could be applied to complex systems of this sort. There were some early efforts to make crude estimates of redox potentials for iron–sulfur clusters [37,56], but, for the most part, quantum chemists focused on spectroscopic issues and ignored redox energetics.

This situation has changed in recent years. First, as discussed above, modern density functional calculations appear able to determine energetics in a much more reliable fashion than was possible before. Second, several approaches to the computation of the response of a solvent or protein environment to a charge change in a solute have been developed that give physically reasonable results. Ichiye and coworkers [124,125] have begun to use microscopic molecular dynamics methods to study the influence of protein and solvent on the redox behavior of rubredoxins. An alternative approach is based on continuum dielectric theory, in which the solute (cluster) is assigned a low dielectric, and the solvent a higher dielectric, characteristic of its static dielectric constant [126,127]. Then the macroscopic Poisson–Boltzmann equation can be solved (numerically or analytically) to obtain an estimate of the solvent polarization response. A similar method treats the solvent as an array of dipoles on a grid, and solves stochastic equations to determine the electrostatic coupling between solvent and charge on the solute [128]. This latter model has recently been used to study the differencs in redox potential among different 4Fe ferredoxin proteins [129,130].

The continuum approach has also recently been used to look at environmental effects on redox potentials in iron–sulfur proteins, specifically contributions to redox potential shifts from sequence variations in related proteins [131,132]. These methods require partial charge models; some of these have been provided through our work [67,70]. More directly, quantum mechanical density functional methods can be combined with solvation terms; we have calculated redox potentials of the 4Fe4S systems $Fe_4S_4(SCH_3)_4^{1-,2-,3-}$ by treating solvation effects through a continuum dielectric model [70]. The solvent contribution to the redox potential can be obtained by calculating the reaction field potential (ϕ^R) from the Poisson–Boltzmann equation, and integrating (1/2) the product of this with the charge density. The charge density was modelled as a set of point charges which give the "best fit" to the electrostatic potential outside the dielectric boundary. These are the electrostatic potential (ESP) charges given in Tables 1 and 2. Then the solvation contribution to the redox potential is given by

$$\Delta E_{PB} = \frac{1}{2}\left(\sum_j q_j^{ox}\,\phi_j^R(\mathrm{ox})\right) - \frac{1}{2}\left(\sum_j q_j^{red}\,\phi_j^R(\mathrm{red})\right) \tag{23}$$

We will summarize some of the most important conclusions here [70]. Overall, the redox potentials for 1Fe, 2Fe and 4Fe systems are predicted with good accuracy, so that there is a good correlation between the predicted potentials for our model systems and synthetic systems in organic solvents. The typical error is between 0.2

and 0.5 eV, compared with contributing energy terms which are much larger (4–9 eV for electronic and solvation (ΔE_{PB}) terms). The spin barycenter concept, discussed earlier, allows us to separate out the specific effects on redox potentials of resonance delocalization and Heisenberg spin coupling from other electronic effects (largely electron–electron repulsion) and from solvation effects (from ΔE_{PB}). The redox potential is decomposed in the following way

$$E^0 = [E_{un}(\text{vac}) + \Delta E_{PB}] + \Delta BT + \Delta JT \tag{24}$$

where the term $E_{un}(\text{vac}) + \Delta E_{PB} = E^0_{un}$ represents the redox potential of the system in the absence of spin coupling and electron delocalization as a sum of the vacuum term plus the solvation energy difference, ΔBT is the resonance delocalization contribution to the redox potential and ΔJT is the Heisenberg spin coupling contribution.

Both Heisenberg spin coupling and resonance delocalization contribute to the much higher redox potential found for the 4Fe high potential couple ($HP_{ox,red}$) compared with the reduced ferredoxin couple ($Fd_{ox,red}$). The effect of the B terms in 4Fe systems is simple and striking, but previously unrecognized. The B term stabilization for Fd_{ox} (or equivalently for HP_{red}) is $10B_m$ because there are two delocalized mixed valence pairs, while that for HP_{ox} and Fd_{red} is only $5B_{ox}$ or $5B_{red}$ because there is only one delocalized pair in each of these. The net result is that the redox potential becomes more positive for the $HP_{ox,red}$ couple (where $\Delta BT = 10B_m - 5B_{ox}$) and more negative for the $Fd_{ox,red}$ couple (where $\Delta BT = 5B_{red} - 10B_m$) because the greater stabilization occurs for the reduced state of HP (positive shift) and for the oxidized state of Fd (negative shift). The ΔJT term also contributes to these shifts, acting in the same direction as ΔBT. Qualitatively, we would expect the $HP_{ox,red}$ redox potential to be more positive than $Fd_{ox,red}$ because the true cluster charges are smaller for the first couple ((1−,2−) vs. (2−,3−)). However, the greater electron–electron repulsion for the (2−,3−) couple in $E_{un}(\text{vac})$ is almost completely compensated by the greater solvation term ΔE_{PB} for (2−,3−) compared with (1−,2−).

For the calculated redox potentials of the HP models, we find the three low-lying electronic states (OS1, OS2, OS3) for the HP_{ox} state with redox potentials $HP_{ox} \rightarrow HP_{red}$ within 0.3 eV, which could contribute to the two redox potential peaks observed by differential pulse polarography in the SR ≡ S(tert-butyl) synthetic system [133]. The HP_{ox} clusters in synthetic systems and in proteins could involve any of these three states. The exact ordering of the ground and low-lying excited states is probably a sensitive function of the ligand (for synthetic systems), and of the protein environment for HP proteins. The close proximity of these states in solvents is similar to their relative energies from vacuum calculations.

4.5. *Phenomenology of spin coupling in* $[Fe_4S_4]^{3-}$ *clusters*

In Section 4.3, we presented a simplified model for spin coupling in which only a single Heisenberg J parameter was used in the spin hamiltonian, along with one or two resonance delocalization terms. These models give a consistent and powerful account of many aspects of iron–sulfur clusters, but are not sufficient to explain all of the interesting spectroscopic features that are encountered. In the next four sections, we will review some of the expected consequences of more complex models that have more than one Heisenberg parameter.

Mössbauer spectroscopy of $[Fe_4S_4]^{3+}$ clusters in proteins and in synthetic analogs shows that the four Fe sites occur in two pairs. The Mössbauer hyperfine spectra show that the effective A values of the mixed valence pair are negative, while those of the diferric pair are positive [75]. This means that the mixed valence pair spin is aligned with the system spin, while the diferric pair spin is oppositely aligned. Consequently, the mixed valence pair spin S_{34} must exceed the diferric pair spin S_{12} in the spin ground state, $S=1/2$. We should then consider whether this is compatible with the high symmetry spin hamiltonian used previously (Eq. (20)) or whether a lower spin symmetry is required. There is another form of the triangle inequality which gives us insight into this question

$$|S-S_{34}| \leqslant S_{12} \leqslant (S+S_{34}) \tag{25}$$

Since the energy $E(S)$ in Eq. (21) is a function only of S_{34} and S, not S_{12}, Eq. (25) shows that there is degeneracy in S_{12}. In particular, for $|S_{34}S\rangle = |9/2, 1/2\rangle$, possible S_{12} values are 4 and 5, but $S_{12}=5$ is incompatible with the signs of the Mössbauer hyperfine parameters. We proposed the following spin hamiltonian

$$H = J_{\text{ox}} \sum_{i<j=1,4} S_i \cdot S_j \pm B(S_{34}+1/2) + \Delta J_{12}(S_1 \cdot S_2) + \Delta J_{34}(S_3 \cdot S_4) \tag{26}$$

with solutions

$$E(S) = (J_{\text{ox}}/2)S(S+1) \pm B(S_{34}+1/2) + (\Delta J_{12}/2)S_{12}(S_{12}+1) \\ + (\Delta J_{34}/2)S_{34}(S_{34}+1) \tag{27}$$

to deal with this problem [108]. To simplify the analysis, we set $\Delta J_{34}=0$, and considered $\Delta J_{12} \geqslant 0$. This means that the diferric pair coupling parameter $J_{12} = J + \Delta J_{12}$ is taken as the largest Heisenberg parameter for the 3+ cubane, and all other Fe–Fe Heisenberg coupling parameters are equal to $J = J_{\text{ox}}$, defined as the Heisenberg parameter governing interlayer Fe–Fe spin coupling. This trend $J(Fe^{3+}\text{–}Fe^{3+}) > J(Fe^{2.5+}\text{–}Fe^{3+}) \geqslant J(Fe^{2.5+}\text{–}Fe^{2.5+})$ (diferric > interlayer ⩾ mixed valence pair) is expected from experimental trends or from calculations on related FeS systems. The B' term was also omitted in this work; the B' term affects the relative energies of different total spin states, but is the same within a given total S value.

Fig. 15 gives the spin state energies $|S_{34}S\rangle$ for $S=1/2, 3/2$ when $\Delta J_{12}=0$, $\Delta J_{34}=0$, so that only a single J and B parameter are used in the hamiltonian. The degeneracies of these states are lifted when $\Delta J > 0$, and the lowest lying spin states $|S_{34}\,S_{12}\,S\rangle$ are shown in Fig. 16. Depending on the $\Delta J/J$ ratio, either $|9/2\;4\;1/2\rangle$ or $|7/2\;3\;1/2\rangle$ becomes the ground spin state. The temperature dependence of the magnetic susceptibility of a synthetic model compound has been analyzed with the

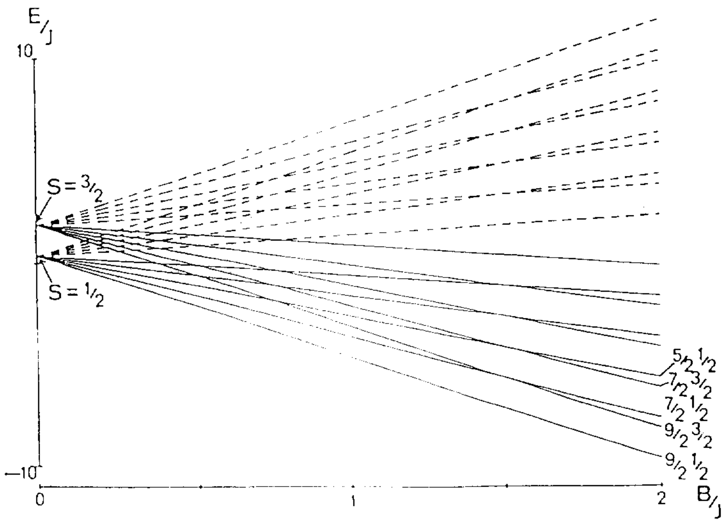

Fig. 15. Spin state energies $E(S)$ for an $[Fe_4S_4(SR)_4]^{1-}$ system (HP_{ox}) with a spin hamiltonian having one B term and one Heisenberg term (J term). Plot of E/J vs. B/J for $S=1/2$ and $S=3/2$. There are degenerate states; these degeneracies are lifted when $\Delta J_{12} \neq 0$. (Reprinted with permission from Ref. [108]. Copyright, American Chemical Society, 1988.)

spin hamiltonian above [134]. (Magnetic susceptibility cannot distinguish between the electronic states OS1, OS2 and OS3.) The best fit to the data gives $B/J=0.9$, $\Delta J_{12}/J=0.22$ and $J=652\ \mathrm{cm}^{-1}$. Recently, we have calculated J, ΔJ_{12} and B for the model system $SR \equiv SCH_3$, in the electronic state OS3, obtaining $J=673\ \mathrm{cm}^{-1}$, $B/J=1.3$ and $\Delta J_{12}/J=0.24$ [135]. The calculation of these three parameters requires the density functional energies of two different broken symmetry states as well as the high-spin state. The calculated results are in good agreement with measurements in the synthetic model system. The states $|9/2\ 4\ 1/2\rangle$ and $|7/2\ 3\ 1/2\rangle$ are close in energy, as shown in Fig. 16. Furthermore, ENDOR proton hyperfine spectra for "hole" sites in the related SR ≡ benzyl-thiolate complex indicate that either of these states can be the ground state depending on the location of the mixed valence pair. Spectroscopically distinguishable signals from ENDOR (proton and Fe hyperfine) and EPR (g tensors) can be correlated with the location of the mixed valence pair on different faces of the cubane [16,17].

4.6. Ligand hyperfine interactions

Ligand hyperfine parameters obey a closely related equation to that for the Fe site, where the intrinsic Fe site hyperfine a_i parameter is replaced by that of the ligand p (a_p) and the observed hyperfine parameter at the ligand is given by A_p ($A_p = K_i a_p$) (Fe_i is the Fe site closest to ligand p, i.e. the Fe site whose spin density controls that of ligand p). This equation applies to the isotropic ligand hyperfine of the ground state, and may be used for comparison with proton ENDOR spectra.

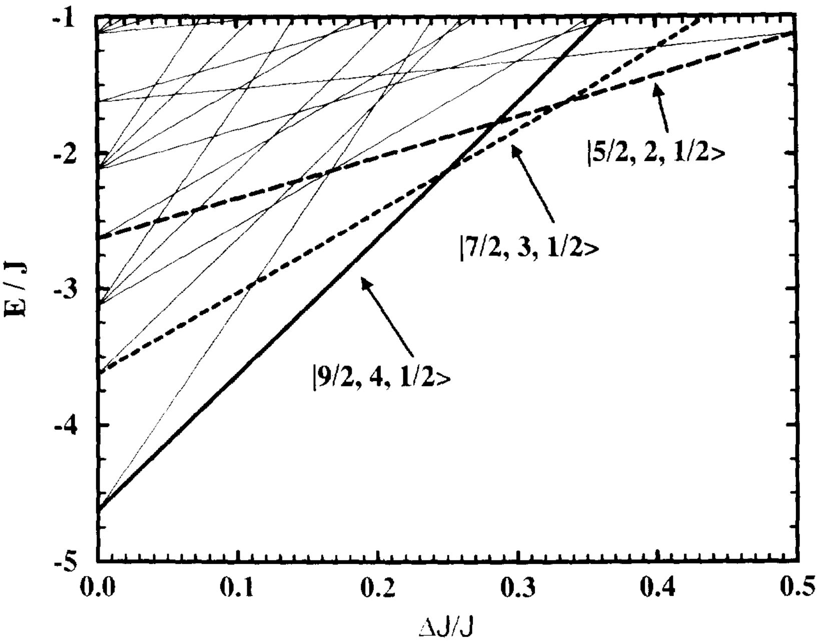

Fig. 16. Low-lying spin states of HP_{ox}, plotting E/J vs. $\Delta J_{12}/J$, where we have chosen $B/J = 1$. Notice the ground state spin crossover from $|9/2\ 4\ 1/2\rangle$ to $|7/2\ 3\ 1/2\rangle$ with increasing $\Delta J_{12}/J$. Notice also the degeneracies at $\Delta J_{12} = 0$. (Redrawn from Ref. [137].)

For comparison with paramagnetic nuclear magnetic resonance (NMR), a thermal ensemble average over accessible spin states is required. For the anisotropic hyperfine, a similar equation applies, but it is advantageous to construct first an effective spin density at the Fe atoms by $D_S(Fe_i) = K_i|\Delta P_i|/2S_i$ (or on sulfurs) from the corresponding spin populations (ΔP_i), since the ligand nucleus has a through-space interaction with the effective "spin coupled" spin density.

The spin distribution in oxidized, high potential (HP) 4Fe4S systems, whether from proteins or from synthetic analogs, has been explored by magnetic Mössbauer (at Fe), ENDOR and paramagnetic NMR spectroscopies, as well as by theoretical calculations [16,75,136,137]. The proton isotropic hyperfine coupling is of considerable value, since this has a geometrical dependence. In particular, the isotropic coupling of the β (methylene) protons is dependent on the corresponding Fe—S—C—H dihedral angle. Recently, we have calculated this angular dependence for a model system $Fe_4S_4(SR)_4^{1-}$ where $R \equiv CH_3$ (electronic state, OS3) and compared these results with ENDOR measurements for the corresponding centers in the synthetic system where R = benzyl. The angular dependence of the low-lying spin states is in good agreement with experimental observations, and this is consistent, both theoretically and experimentally, with a π-type spin distribution on the terminal sulfurs with respect to the corresponding Fe—S bonds [137]. Further theoretical and experimental work is in progress.

4.7. Spin states and valence trapping in reduced 4Fe4S and 4Fe4Se complexes

The methods above are based on a pairwise equivalence picture which is also consistent with the electronic symmetry C_{2v} for $[Fe_4S_4(SR)_4]^{1-,2-,3-}$ complexes in D_{2d} or C_{2v} geometries. However, there may be other environmental or geometric asymmetries where a pairwise equivalence model or "dimer of dimers" model is no longer valid. In particular, it may be possible to lower the cluster symmetry from pairwise equivalence (2:2) to having a single site which is differentiated from the other Fe sites to make 3:1 or 2:1:1 site equivalence patterns. This is described by the phenomenological model discussed next.

A spin coupling model has been described that allows for lower symmetry for reduced $[Fe_4S_4]^{1+}$ and $4Fe4Se^{1+}$ proteins and synthetic analogs [111,138]. The elements of the model are two different Heisenberg (J_1, J_2) parameters for all formal mixed valence (Fe^{3+}–Fe^{2+}) and ferrous pairs (Fe^{2+}–Fe^{2+}) respectively, delocalization within a single mixed valence pair (described by a single B parameter) and an external site asymmetry energy favoring electron trapping. In this model, the six Fe–Fe pair Heisenberg interactions are divided into a 3:3 ratio (three mixed valence pairs and three ferrous pairs); this is in contrast with the previous models where either all Heisenberg pairs are the same (6:0, one J parameter) or some are different (4:1:1, three J parameters; 5:1, two J parameters). Direct application of Racah spin algebra to this model shows that spin crossover from delocalized $S = 1/2$ (with pairwise site equivalence, 2:2) and $S = 3/2$ states to a valence trapped $S = 7/2$ state (3:1 site equivalence) is quite feasible, as is observed in reduced $4Fe4Se^{1+}$ clusters of Se substituted clostridial ferredoxin [139,140]. This is illustrated in Figs. 17 and 18. The region of stability of $S = 7/2$ compared with $S = 1/2$ is greater for the trapping parameter $f_{loc} = 5$ compared with $f_{loc} = 0$, shown in Figs. 17 and 18 respectively. Recently, we have found good evidence that the P^{OX} state of the Fe_8S_8 cluster in nitrogenase FeMo proteins contains an $S = 1/2$ cubane coupled to an $S = 7/2$ cubane, showing the broader relevance of this situation (discussed below).

4.8. Analysis of hyperfine interactions and spin states in nitrogenase P clusters

The P clusters of nitrogenase are Fe_8S_8 superclusters which are an important part of the FeMo protein. Their expected role is to transfer electrons to the catalytic FeMo cofactor, where binding and reduction of molecular nitrogen to ammonia occur [141]. Two oxidation states of the P cluster that have been examined in some detail are P^N (N = native, the normal resting state) [142–144] and P^{OX} which is oxidized by two electrons with respect to P^N [145–147]. P^{OX} has been studied by both magnetic Mössbauer and integer spin EPR spectroscopy. We have recently proposed a spin coupling model for oxidized P clusters [109], including both the alignment of Fe site spins and sequence specific assignments of Fe valences

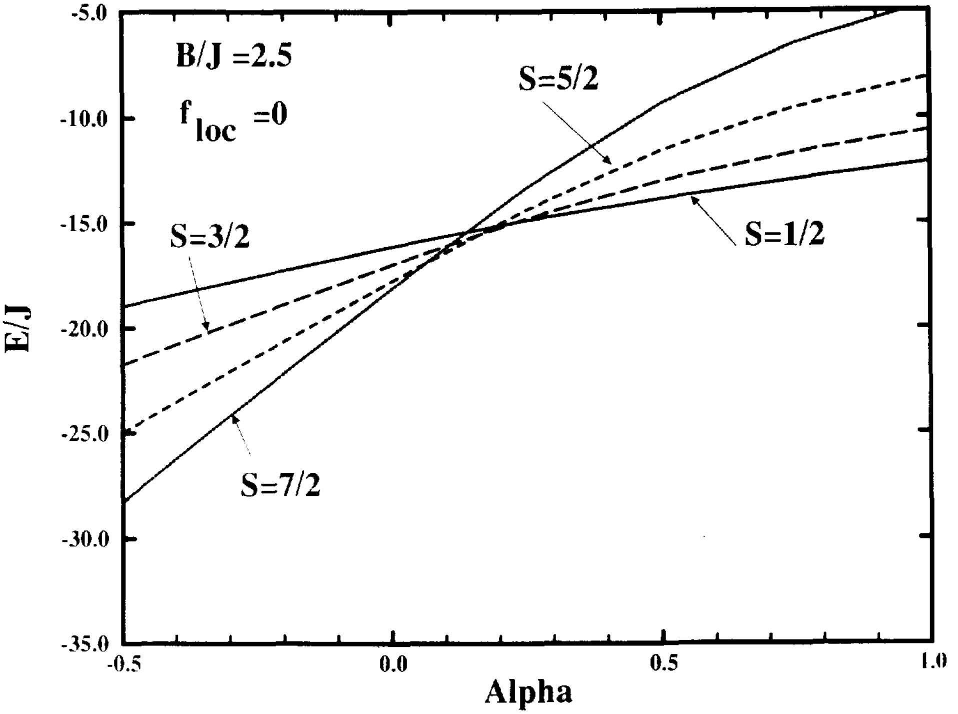

Fig. 17. Each subunit of P^{OX} has a formal oxidation state $[Fe_4S_4]^{1+}$. The spin state energies of a delocalized (1+) cluster were determined from a spin hamiltonian with four different parameters, J_2 for all pairwise Fe^{2+}–Fe^{2+} Heisenberg coupling interactions, J_1 for all pairwise Fe^{2+}–Fe^{3+} Heisenberg interactions and a single resonance delocalized mixed valence pair with resonance parameter B. The parameter $\alpha = J_2/J_1$ and E/J_1 is plotted vs. α for the lowest energy $S = 1/2$, $3/2$, $5/2$ and $7/2$ states (one of each spin type). The scaled localization energy parameter $f_{loc} = E_{loc}/B$, where E_{loc} is the difference in site energies within the mixed valence pair. Here $f_{loc} = 0$. (Reprinted with permission from Ref. [109]. Copyright, American Chemical Society, 1994. See also Refs. [111,138].)

(Fe^{2+}, Fe^{3+}, $Fe^{2.5+}$) to the 2(Fe_4S_4) subclusters, based on the analysis of magnetic Mössbauer hyperfine data [145,146] and EPR spectra [147].

In our model, each half of the cluster is formally equivalent to a classic $[Fe_4S_4]^{1+}$ unit formally containing one ferric and three ferrous ions. However, due to the presence of an additional serine ligand at one iron site, the spin properties of the two halves are distinct; one has a typical spin $S_1 = 1/2$ and the other, close to the serine, a spin $S_2 = 7/2$. Cubane 1 has a delocalized mixed valence pair and a ferrous pair, while cubane 2 exhibits trapped valence (Fe^{3+}, Fe^{2+}). The rationale for an $S_i = 1/2$ to $S_i = 7/2$ spin crossover being connected with valence trapping was discussed in the previous section. A parallel coupling of these two subspins (resulting in the state $|S_1, S_2, S_t\rangle$ with S_t equal to 4) is found to be more likely than the antiparallel $|1/2, 7/2, 3\rangle$. The overall spin alignment is illustrated in Fig. 19.

This conclusion is based on three lines of evidence. First, a spin coupling framework is developed which relates observed site hyperfine values for the entire Fe_8S_8 cluster

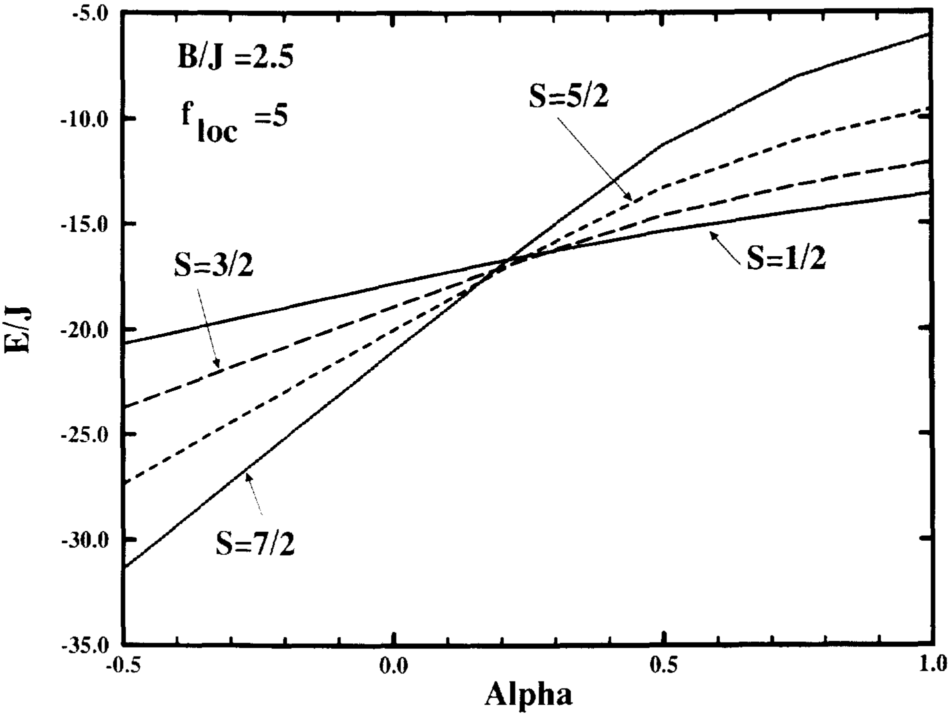

Fig. 18. The spin state energies of a (1+) cluster in the presence of site inequivalence (static trapping) within the mixed valence pair, $f_{loc} = 5$; all other parameters as in Fig. 17. (Reprinted with permission from Ref. [109]. Copyright, American Chemical Society, 1994. See also Refs. [111,138].)

to those typically observed in simpler cubane subunits by using spin projection coefficients. This acts as a sieve on possible spin coupling schemes, eliminating most of these. Second, the ferrous ions (identified from their large isomer shifts) present both positive and negative hyperfine parameters, which points to a ferromagnetic coupling of the two cubane subspins S_1 and S_2. Third, we propose the use of a simple empirical quantity a_{test} equal to the sum of A_i over all 8Fe sites. Comparison of the values of a_{test} (which is markedly spin dependent) for P clusters from *Clostridium pasteurianum* (Cp) and from *Azotobacter vinelandii* (Av) with theoretical estimates for the possible parallel coupled states $|1/2, 5/2, 3\rangle$ and $|1/2, 7/2, 4\rangle$ clearly favors the latter. Our spin coupling model predicts a 5:3 (5 negative and 3 positive) pattern for the hyperfine parameters, rather than 4:4 as originally measured in Av or 6:2 as in Cp (and also in Av after experimental reanalysis) [145–147]. Analysis of Mössbauer hyperfine data can be ambiguous about the signs of some hyperfine parameters in complicated cases, while it can be completely definitive in simpler situations. Integer spin EPR indicates that the total system spin is either $S = 3$ or 4 (or possibly a quantum mixture of these) for nitrogenase P clusters from various species (*Xanthobacter autotrophicus* (Xa1), Av1, *Klebsiella pneumoniae* (Kp1)) [147], while our analysis supports $S = 4$ for Av1 and Cp1. Thus our proposal resolves

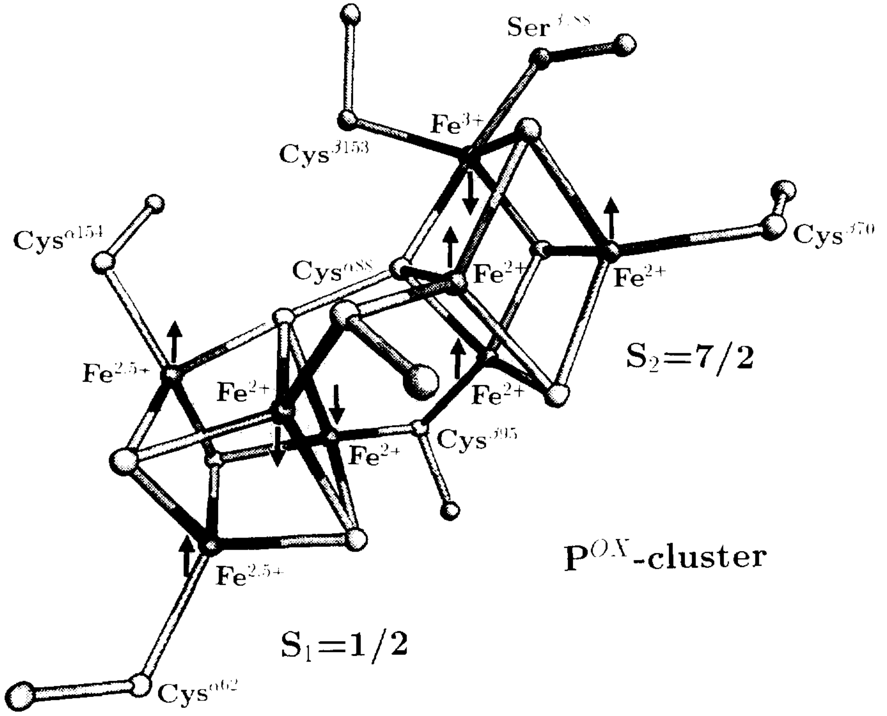

Fig. 19. The P cluster structure is taken from the X-ray structure of Kim and Rees [142,143] for the resting state of the cluster P^N. A model for valence assignments of the different Fe sites and for the alignment of Fe site spin vectors was obtained by analysis of Mössbauer internal magnetic fields, and from other Mössbauer and EPR measurements for oxidation state P^{OX} which is a paramagnetic integer spin system. P^{OX} is $2e^-$ oxidized with respect to the resting from P^N. (Reprinted with permission from Ref. [109]. Copyright, American Chemical Society, 1994.)

current ambiguities in experimental data, while being clearly testable by future more definitive EPR, Mössbauer, and magnetic circular dichroism (MCD) experiments. This sort of analysis illustrates some of the power of the spin projection "algebra" outlined in Section 3.3.

4.9. *Vibronic coupling*

There are various possible sources of asymmetry in polynuclear transition metal complexes. One of these is vibronic coupling [24,97,99,115,148]. We expect that different Fe oxidation states within a particular complex will have different Fe—S,S* bond lengths and bond angles at the energy minimum, and that this will compete with valence delocalization. The vibronic distortion is governed by an electron–nuclear coupling parameter λ, by the Fe–S force constant (k, usually assumed to be for an Fe–S stretch mode) and by valence delocalization (for example, by $B(S_{ij}+1/2)$ in a mixed valence dimer). In a dimer, when $|B(S_{ij}+1/2)| > \lambda^2/2k$, the system remains delocalized, and the upper (u) and lower (g) potential energy surfaces of the system are nested harmonic surfaces; for $\lambda^2/2k$ larger than the resonance energy, a double well lower potential energy surface develops, and the excess electron becomes trapped, with a correlated bond length distortion [24]. Such vibronic coupling models have now been developed for mixed valence 2Fe2S, 3Fe4S and (high potential) 4Fe4S systems. These models give insights into electron trapping onto pairs of sites with electron delocalization within a pair for 3Fe and 4Fe systems, and into the trapped site valence observed in 2Fe systems [24,97,99,115,148]. The relative importance of vibronic coupling vs. coupling to solvent or hydrogen bonding in determining electron localization–delocalization is still an open question. Also, there are a variety of geometric distortions that may be relevant beyond the Fe—S,S* bond lengths. Finally, we note that the *B* parameters linking different Fe–Fe pairs can differ, and are dependent on the orbital electronic state of the system (for example, *B* vs. *B*′). Future models will have to deal with these important factors.

5. Conclusions

Our purpose in this review has been to demonstrate the close interconnection between orbital interactions and spin coupling in iron–sulfur complexes. We have emphasized some basic themes. First, spin polarization effects are strong for these high-spin transition metal sites, and this affects the relative energies of iron compared with mainly sulfur based levels, and leads to an inverted energy level scheme. Second, because of the compact Fe(3d) shell, electron relaxation effects are also strong, so that redox events affect the net charges mainly on bridging and terminal sulfurs, and the anisotropy of the charge distribution on iron. Third, Heisenberg coupling and valence electron delocalization (resonance delocalization or double exchange) compete; the large number of spin states possible in polynuclear systems provides a way for effective pairwise valence delocalization over mixed valence pairs in 3Fe4S and 4Fe4S complexes. A strong resonance delocalization energy requires parallel (or nearly parallel) spins within a mixed valence pair (or pairs). Valence electron delocalization over an entire $[Fe_4S_4]^{1+}$ cluster is possible, but this is more easily disrupted by external asymmetries than pairwise delocalization. Fourth, Heisenberg spin coupling and resonance delocalization can contribute significantly to the comparative redox potentials of different clusters and oxidation states. Solvation effects can compensate even for large differences in electron–electron repulsion among different redox couples. External asymmetries, from the coordination environment, from solvation or from the protein environment can strongly affect spin states and spectroscopic properties, with significant effects on cluster energetics as well. In this work, we have emphasized the value of broken symmetry density functional calculations and spin projection methods both for extracting relevant spin coupling, electron delocalization and other spectroscopic parameters, and as tools for understanding the underlying physical phenomena. At a more phenomenological level, spin projection coefficients provide a valuable means for evaluating patterns of spin coupling in complex polynuclear systems. The power of the computational tools now available to examine these and other aspects of iron–sulfur clusters is impressive, and we expect to see significant progress in the next few years.

Acknowledgements

We thank J.L. Chen and D. Bashford for their contributions to the work on redox potentials and solvation, and E.J. Baerends for use of the ADF density functional programs. We thank the group at CEN, Grenoble, particularly B. Lamotte, J. Jordanov and J. Gaillard, for helpful discussions. This work was supported by NIH grant GM39914 and by a NATO travel grant CRG-910204.

References

[1] H. Beinert, FASEB J., 4 (1990) 2483–2491.
[2] P. Mitchell, J. Biochem., 97 (1985) 1–18.
[3] A.L. Han, T. Yagi and Y. Hatefi, Arch. Biochem. Biophys., 275 (1989) 166–173.
[4] J.H. Golbeck, Biochim. Biophys. Acta, 895 (1987) 167–204.
[5] R.L. Switzer, BioFactors, 2 (1989) 77–86.
[6] M.C. Kennedy and C.D. Stout, Adv. Inorg. Chem., 38 (1992) 323–339.
[7] B.K. Burgess, in T.G. Spiro (ed.), Molybdenum Enzymes, Wiley, New York, 1985, pp. 161–219.
[8] R.A. Scott, P.M. Li and S.I. Chan, Ann. N.Y. Acad. Sci., 550 (1988) 53.
[9] D.H. Kim, R.D. Britt, M.P. Klein and K. Sauer, J. Am. Chem. Soc., 112 (1990) 9389.
[10] G.W. Brudvig, W.F. Beck and J.C. de Paula, Annu. Rev. Biophys. Biophys. Chem., 18 (1989) 25–46.
[11] W. Lovenberg (ed.), Iron–Sulfur Proteins, Academic Press, New York, 1977.
[12] T.G. Spiro (ed.), Iron–Sulfur Proteins, Wiley, New York, 1982.
[13] R. Cammack and A.G. Sykes (eds.), Iron–Sulfur Proteins, Academic Press, San Diego, 1992.
[14] J.A. Ibers and R.H. Holm, Science, 209 (1980) 223–235.
[15] E.P. Day, J. Peterson, J.J. Bonvoisin, I. Moura and J.J.G. Moura, J. Biol. Chem., 263 (1988) 3684–3689.
[16] J.-M. Mouesca, G. Rius and B. Lamotte, J. Am. Chem. Soc., 115 (1993) 4714–4731.
[17] J. Gloux, P. Gloux, B. Lamotte, J.-M. Mouesca and G. Rius, J. Am. Chem. Soc., 116 (1994) 1953–1961.
[18] K. Sauer, Acc. Chem. Res., 13 (1980) 249.
[19] K. Wieghardt, Angew. Chem. Int. Ed. Engl., 33 (1994) 725–728.
[20] J.B. Vincent, G.L. Olivier-Lilley and B.A. Averill, Chem. Rev., 90 (1990) 1447–1467.
[21] S. Pulver, W.A. Froland, B.G. Fox, J.D. Lipscomb and E.I. Solomon, J. Am. Chem. Soc., 115 (1993) 12409–12422.
[22] J.S. Griffith, Struct. Bonding, 10 (1972) 87.
[23] A. Bencini and S. Midollini, Coord. Chem. Rev., 120 (1992) 87–136.
[24] G. Blondin and J.J. Girerd, Chem. Rev., 90 (1990) 1359–1376.
[25] J.K. McCusker, E.A. Schmitt and D.N. Hendrickson, in D. Gatteschi (ed.), Magnetic Molecular Materials, Kluwer Press, Leiden, 1991.
[26] P.J. Hay, J.C. Thibeault and R. Hoffman, J. Am. Chem. Soc., 97 (1975) 4884.
[27] H. Astheimer and W. Haase, J. Chem. Phys., 85 (1986) 1427.
[28] F. Nepveu, W. Haase and H. Astheimer, J. Chem. Soc., Faraday Trans. 2, 82 (1986) 551–565.
[29] P. de Loth, P. Cassoux, J.P. Daudey and J.P. Malrieu, J. Am. Chem. Soc., 103 (1981) 4007.
[30] O. Kahn, Angew. Chem. Int. Ed. Engl., 24 (1985) 834.
[31] P. de Loth, P. Karafiloglou, J.P. Daudey and O. Kahn, J. Am. Chem. Soc., 110 (1988) 5676.

[32] A. Bencini and D. Gatteschi, J. Am. Chem. Soc., 1089 (1986) 5763.

[33] C. Albonico and A. Bencini, Inorg. Chem., 27 (1988) 1934.

[34] P.K. Ross and E.I. Solomon, J. Am. Chem. Soc., 113 (1991) 3246–3259.

[35] B.A. Averill, T. Herskovitz, R.H. Holm and J.A. Ibers, J. Am. Chem. Soc., 95 (1973) 3523–3534.

[36] A.J. Thomson, J. Chem. Soc. Dalton Trans., (1981) 1180–1189.

[37] B.A. Bair and W.A. Goddard, J. Am. Chem. Soc., 100 (1978) 5669.

[38] J.G. Norman, Jr. and S.C. Jackels, J. Am. Chem. Soc., 97 (1975) 3833–3835.

[39] J.G. Norman, Jr., B.J. Kalbacher and S.C. Jackels, J. Chem. Soc., Chem. Commun., (1978) 1027–1029.

[40] J.G. Norman, Jr., P.B. Ryan and L. Noodleman, J. Am. Chem. Soc., 102 (1980) 4279–4282.

[41] A. Aizman and D.A. Case, J. Am. Chem. Soc., 104 (1982) 3269–3279.

[42] L. Noodleman, D.A. Case and E.J. Baerends, in J.K. Labanowski and J.W. Andzelm (eds.), Density Functional Methods in Chemistry, Springer-Verlag, New York, 1991, pp. 109–123.

[43] T. Ziegler, Chem. Rev., 91 (1991) 651–667.

[44] J.K. Labanowski and J.W. Andzelm (eds.), Density Functional Methods in Chemistry, Springer-Verlag, New York, 1991.

[45] C. Sosa, J. Andzelm, B.C. Elkin, E. Wimmer, K.D. Dobbs and D.A. Dixon, J. Phys. Chem., 96 (1992) 6630–6636.

[46] T. Ziegler and J. Li, Can. J. Chem., 72 (1994) 783–789.

[47] T.V. Russo, R.L. Martin and P.J. Hay, J. Chem. Phys., 101 (1994) 7729–7737.

[48] B.G. Johnson, P.M.W. Gill and J.A. Pople, J. Chem. Phys., 98 (1993) 5612–5626.

[49] G. te Velde and E.J. Baerends, J. Comp. Phys., 99 (1992) 84–98.

[50] D.H. Jones, A.S. Hinman and T. Ziegler, Inorg. Chem., 32 (1993) 2092–2095.

[51] A. Rosa and E.J. Baerends, Inorg. Chem., 33 (1994) 584–595.

[52] E.A. Schmitt, L. Noodleman, E.J. Baerends and D.N. Hendrickson, J. Am. Chem. Soc., 114 (1992) 6109–6119.

[53] B.V. DePamphilis, B.A. Averill, T. Herskovitz, L. Que and R.H. Holm, J. Am. Chem. Soc., 96 (1974) 4159–4167.

[54] R.H. Holm, Adv. Inorg. Chem., 38 (1992) 1–71.

[55] L. Noodleman and D.A. Case, Adv. Inorg. Chem., 38 (1992) 423–470.

[56] L. Noodleman and E.J. Baerends, J. Am. Chem. Soc., 106 (1984) 2316–2327.

[57] J.E. Huheey, Inorganic Chemistry, Harper and Row International, 2nd edn., 1979, pp. 839–851.

[58] D.F. Shriver, P.W. Atkins and C.H. Langford, Inorganic Chemistry, W.H. Freeman, New York, 1990.

[59] F.A. Cotton and G. Wilkinson, Advanced Inorganic Chemistry, Wiley-Interscience, New York, 5th edn., 1988.

[60] A. Rosa and E.J. Baerends, New J. Chem., 15 (1991) 815–829.

[61] R.L. DeKock, E.J. Baerends and R. Hengelmolen, Organometallics, 3 (1984) 289–292.

[62] K.D. Butcher, S.V. Didziulis, B. Briat and E.I. Solomon, J. Am. Chem. Soc., 112 (1990) 2231.

[63] K.D. Butcher, M.S. Gebhard and E.I. Solomon, Inorg. Chem., 29 (1990) 2067.

[64] M.S. Gebhard, J.C. Deaton, S.A. Koch, M. Millar and E.I. Solomon, J. Am. Chem. Soc., 112 (1990) 2217.

[65] M.S. Gebhard, S.A. Koch, M. Millar, F.J. Devlin, P.J. Stephens and E.I. Solomon, J. Am. Chem. Soc., 113 (1991) 1640–1649.

[66] T. Ziegler, A. Rauk and E.J. Baerends, Chem. Phys., 16 (1976) 209–217.

[67] L. Noodleman, J.G. Norman, Jr., J.H. Osborne, A. Aizman and D.A. Case, J. Am. Chem. Soc., 107 (1985) 3418–3426.

[68] J.N. Butt, A. Sucheta, L.L. Martin, B. Shen, B.K. Burgess and F.A. Armstrong, J. Am. Chem. Soc., 115 (1993) 12 587–12 588.

[69] J.L. Chen, L. Noodleman, D.A. Case and D. Bashford, J. Phys. Chem., 98 (1994) 11 059–11 068.

[70] J.-M. Mouesca, J.L. Chen, L. Noodleman, D. Bashford and D.A. Case, J. Am. Chem. Soc., 116 (1994) 11 898–11 914.

[71] C.M. Breneman and K.B. Wiberg, J. Comp. Chem., 11 (1990) 361–373.

[72] L.E. Chirlian and M.M. Francl, J. Comp. Chem., 8 (1987) 894–905.

[73] B.H. Besler, K.M. Merz, Jr. and P.A. Kollman, J. Comp. Chem., 11 (1990) 431–439.
[74] P. Middleton, D.P.E. Dickson, C.E. Johnson and J.D. Rush, Eur. J. Biochem., 88 (1978) 135–141.
[75] V. Papaefthymiou, M.M. Millar and E. Münck, Inorg. Chem., 25 (1986) 3010–3014.
[76] P.O. Lowdin, Phys. Rev., 97 (1955) 1509.
[77] (a) P.O. Lowdin, Rev. Mod. Phys., 34 (1962) 80.
(b) C.A. Coulson and I. Fischer, Phil. Mag., 40 (1949) 386.
[78] R.K. Nesbet, Ann. Phys., 3 (1958) 397.
[79] R.K. Nesbet, Ann. Phys., 4 (1958) 87.
[80] P.W. Anderson, in G.T. Rado and H. Suhl (eds.), Magnetism, Academic Press, New York, 1963, pp. 25–83.
[81] P.W. Anderson, Phys. Rev., 115 (1959) 2.
[82] P.J. Hay, J. Am. Chem. Soc., 100 (1978) 2897.
[83] H. Fukatome, Prog. Theor. Phys., 47 (1972) 1156.
[84] L. Noodleman and J.G. Norman, Jr., J. Chem. Phys., 70 (1979) 4093.
[85] M. Benard, J. Chem. Phys., 71 (1979) 2546.
[86] L. Noodleman, J. Chem. Phys., 74 (1981) 5737.
[87] E.I. Solomon, F. Tuczek, D.E. Root and C.A. Brown, Chem. Rev., 94 (1994) 827–856.
[88] K. Yamaguchi, T. Fueno, N. Ueyama, A. Nakamura and M. Ozaki, Chem. Phys. Lett., 164 (1989) 210.
[89] J.R. Hart, A.K. Rappe, S.M. Gorun and T.H. Upton, Inorg. Chem., 31 (1992) 5254–5259.
[90] J.R. Hart, A.K. Rappé, S.M. Gorun and T.H. Upton, J. Phys. Chem., 96 (1992) 6264–6269.
[91] L. Noodleman and E.R. Davidson, Chem. Phys., 109 (1986) 131–143.
[92] L. Noodleman, D.A. Case and A.J. Aizman, J. Am. Chem. Soc., 110 (1988) 1001–1005.
[93] S.F. Sontum, L. Noodleman and D.A. Case, in D.R. Salahub and M.C. Zerner (eds.), The Challenge of d and f Electrons: Theory and Computation, American Chemical Society, Washington, DC, 1989, pp. 366–377.
[94] L. Noodleman, D.A. Case and S.F. Sontum, J. Chim. Phys., 86 (1989) 743–755.
[95] P.W. Anderson and H. Hasegawa, Phys. Rev., 100 (1955) 675–681.
[96] C. Zener, Phys. Rev., 82 (1951) 403.
[97] J.J. Girerd, J. Chem. Phys., 79 (1983) 1766–1775.
[98] V. Papaefthymiou, J.J. Girerd, I. Moura, J.J.G. Moura and E. Münck, J. Am. Chem. Soc., 109 (1987) 4703–4710.
[99] E.L. Bominaar, S.A. Borshch and J.J. Girerd, J. Am. Chem. Soc., 116 (1994) 5362–5372.
[100] R.H. Sands and W.R. Dunham, Q. Rev. Biophys., 7 (1975) 443–504.
[101] E. Merzbacher, Quantum Mechanics, Wiley, New York, 2nd edn., 1970, pp. 389–404.
[102] D.M. Brink and G.R. Satchler, Angular Momentum, Oxford University Press, 2nd edn., 1968.
[103] P. Bertrand, Inorg. Chem., 32 (1993) 741–745.
[104] J.F. Gibson, D.O. Hall, J.H.M. Thornley and F.R. Whatley, Proc. Natl. Acad. Sci. USA, 56 (1966) 987–989.
[105] B. Guigliarelli, P. Bertrand and J.-P. Gayda, J. Chem. Phys., 85 (1986) 1689–1692.
[106] J.T. Sage, Y.-M. Xia, P.G. Debrunner, D.T. Keough, J. de Jersey and B. Zerner, J. Am. Chem. Soc., 111 (1989) 7239–7247.
[107] P. Middleton, D.P.E. Dickson, C.E. Johnson and J.D. Rush, Eur. J. Biochem., 104 (1980) 289–296.
[108] L. Noodleman, Inorg. Chem., 27 (1988) 3677–3679.
[109] J.-M. Mouesca, L. Noodleman and D.A. Case, Inorg. Chem., 33 (1994) 4819–4830.
[110] B.H. Huynh, J.J.G. Moura, I. Moura, T.A. Kent, J. LeGall, A.V. Xavier and E. Münck, J. Biol. Chem., 255 (1980) 3242.
[111] L. Noodleman, Inorg. Chem., 30 (1991) 246–256.
[112] J.-M. Mouesca, L. Noodleman and D.A. Case, manuscript in preparation.
[113] B.C. Antanaitis and T.H. Moss, Biochim. Biophys. Acta, 405 (1875) 262.
[114] T.A. Kent and E. Münck, Hyp. Int., 27 (1986) 161–172.
[115] S.A. Borshch, E.L. Bominaar, B. Blondin and J.J. Girerd, J. Am. Chem. Soc., 115 (1993) 5155–5168.

[116] K.K.P. Srivastava, K.K. Surerus, R.C. Conover, M.K. Johnson, J.-B. Park, M.W.W. Adams and E. Münck, Inorg. Chem., 32 (1993) 927–936.
[117] J. Zhou, M.J. Scott, Z. Hu, G. Peng, E. Münck and R.H. Holm, J. Am. Chem. Soc., 114 (1992) 10843–10854.
[118] M. Tinkham, Group Theory and Quantum Mechanics, McGraw-Hill, New York, 1964, pp. 167–170, 299–309.
[119] E.B. Wilson, J.C. Decius and P.C. Cross, Molecular Vibrations, Dover, New York, 1980, pp. 312–346.
[120] M.M. Maltempo, J. Chem. Phys., 61 (1974) 2540–2547.
[121] M.J. Carney, G.C. Papaefthymiou, K. Spartalian, R.B. Frankel and R.H. Holm, J. Am. Chem. Soc., 110 (1988) 6084–6095.
[122] P.A. Lindahl, E.P. Day, T.A. Kent, W.H. Orme-Johnson and E.J. Münck, Biol. Chem., 260 (1985) 11160–11173.
[123] M.B. Robin and P. Day, Adv. Inorg. Chem. Radiochem., 10 (1967) 247.
[124] Y. Yang, B.W. Beck, V.S. Shenoy and T. Ichiye, J. Am. Chem. Soc., 115 (1993) 7439–7444.
[125] V.S. Shenoy and T. Ichiye, Proteins, 17 (1993) 152–160.
[126] D. Bashford, Curr. Op. Struct. Biol., 1 (1991) 175–184.
[127] B. Honig, K. Sharp and A.-S. Yang, J. Phys. Chem., 97 (1993) 1101–1109.
[128] A. Warshel and J. Aqvist, Annu. Rev. Biophys. Chem., 20 (1991) 267–298.
[129] R. Langen, G.M. Jensen, U. Jacob, P.J. Stephens and A. Warshel, J. Biol. Chem., 267 (1992) 25625–25627.
[130] G.M. Jensen, A. Warshel and P.J. Stephens, Biochemistry, 33 (1994) 10911–10924.
[131] C.C. Correll, M.L. Ludwig, C.M. Bruns and P.A. Karplus, Protein Sci., 2 (1993) 2112–2133.
[132] E.T. Smith, J.M. Tomich, T. Iwamoto, J.H. Richards, Y. Mao and B.A. Feinberg, Biochemistry, 30 (1991) 11669–11676.
[133] P.K. Mascharak, K.S. Hagen, J.T. Spence and R.H. Holm, Inorg. Chim. Acta, 80 (1983) 157–170.
[134] J. Jordanov, E.K.H. Roth, P.H. Fries and L. Noodleman, Inorg. Chem., 29 (1990) 4288–4292.
[135] J.-M. Mouesca, L. Noodleman and D.A. Case, Int. J. Quantum Chem., in press.
[136] L. Banci, I. Bertini, S. Ciurli, S. Ferretti, C. Luchinat and M. Piccioli, Biochemistry, 32 (1993) 9387–9397.
[137] L. Noodleman, J.-L. Chen, D.A. Case, C. Giori, G. Rius, J.M. Mouesca and B. Lamotte, in G.N. LaMar (ed.), NMR of Paramagnetic Macromolecules, Kluwer Scientific, Leiden, 1994.
[138] L. Noodleman, Inorg. Chem., 30 (1991) 256–264.
[139] P. Auric, J. Gaillard, J. Meyer and J.M. Moulis, Biochem. J., 242 (1987) 525–530.
[140] J. Gaillard, J.M. Moulis, P. Auric and J. Meyer, Biochemistry, 25 (1986) 464.
[141] W.H. Orme-Johnson, Science, 257 (1992) 1639–1640.
[142] M.K. Chan, J. Kim and D.C. Rees, Science, 260 (1993) 792–794.
[143] J. Kim and D.C. Rees, Science, 257 (1992) 1677–1682.
[144] J.T. Bolin, N. Campobasso, S.W. Muchmore, T.V. Morgan and L.E. Mortenson, in E.I. Steifel, D. Coucoucanis and W.E. Newton (eds.), Molybdenum Enzymes, Cofactors, and Model Systems, American Chemical Society, Washington, DC, 1993, pp. 186–195.
[145] R. Zimmermann, E. Münck, W.J. Brill, V.K. Shah, M.T. Henzl, J. Rawlings and W.H. Orme-Johnson, Biochim. Biophys. Acta, 537 (1978) 185–207.
[146] B.H. Huynh, M.T. Henzl, J.A. Christner, R. Zimmermann, W.H. Orme-Johnson and E. Münck, Biochim. Biophys. Acta, 623 (1980) 124.
[147] K.K. Surerus, M.P. Hendrich, P.D. Christie, D. Rottgardt, W.H. Orme-Johnson and E. Münck, J. Am. Chem. Soc., 114 (1992) 8579–8590.
[148] S.A. Borshch and L.F. Chibotaru, Chem. Phys., 135 (1989) 375–380.